Journal Pre-proof

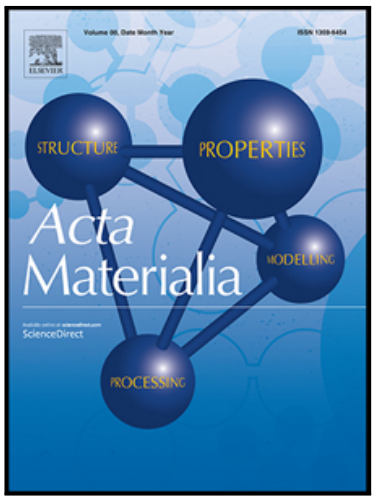

Evolution of texture and intergranular stresses of αZr and minority phases in Zr-2.5Nb pressure tube through synchrotron X-ray diffraction

M.A. Vicente Alvarez , Constanza Buioli , J. Santisteban , P. Vizcaino

PII: S1359-6454(24)00154-X
DOI: https://doi.org/10.1016/j.actamat.2024.119802
Reference: AM 119802

To appear in: *Acta Materialia*

Received date: 22 August 2023
Revised date: 26 February 2024
Accepted date: 27 February 2024

Please cite this article as: M.A. Vicente Alvarez , Constanza Buioli , J. Santisteban , P. Vizcaino , Evolution of texture and intergranular stresses of αZr and minority phases in Zr-2.5Nb pressure tube through synchrotron X-ray diffraction, *Acta Materialia* (2024), doi: https://doi.org/10.1016/j.actamat.2024.119802

Evolution of texture and intergranular stresses of αZr and minority phases in Zr-2.5Nb pressure tube through synchrotron X-ray diffraction

M.A. Vicente Alvarez[1,2], Constanza Buioli[3,4], J. Santisteban[1,2], P. Vizcaino[2,3]

1 Laboratorio Argentino de Haces de Neutrones, Centro Atómico Bariloche, CNEA, Argentina
2 Consejo Nacional de investigaciones Científicas y Técnicas, CONICET, Argentina
3 Zirconium Technology Department, Centro Atómico Ezeiza, CNEA, Argentina.
4 Instituto Sábato, Universidad Nacional de San Martín Centro Atómico Constituyentes, Buenos Aires, CNEA, Argentina

Keywords: crystallographic texture, intergranular stress, Zr-Nb pressure tube, X-Ray diffraction

Abstract

This study investigates the impact of different processing steps on the crystallographic texture evolution of αZr and minority phases βZr and ωZr, and intergranular stresses as a function of grain orientation in a Zr2.5Nb pressure tube. This was done by analysis of diffraction data recorded in the 1-ID line of the Advanced Photon Source for high energy X-Rays (~80Kev) in transmission geometry on three samples with different processing conditions: extruded, cold rolled and after autoclaving. The crystallographic texture of both αZr and βZr phases changes slightly after cold rolling, with the Burgers orientation relationship between the two phases remaining intact. The texture of βZr and ωZr shows that βZr decomposition during thermal treatment is sensitive to grain orientation. A new method was proposed to obtain the orientation dependence of the intergranular stresses from the experimental pole figures. Intergranular stresses in αZr grains were low after extrusion, but rolling significantly increased them, with values with magnitude as higher as 350 MPa and a strong dependence on grain orientation. The autoclaving treatment leads to important stress relaxation, but the dependence on grain orientation remains. The βZr phase grains exhibit significant intergranular strains in both extruded and cold-rolled conditions; the hydrostatic part was associated the presence of Nb in solid solution, with content of ~20% and an orientation dependence of approximately ±1 at%. The deviatoric strain was attributed to intergranular stresses, with stresses below 80 MPa for the extruded sample and ranging from -600 to 400 MPa after cold rolling.

1. Introduction

Pressure tubes are critical Zr-based components located in the core of CANDU nuclear power reactors. These tubes' service life is primarily defined by irradiation growth and delayed hydride cracking mechanisms, which are influenced by metallurgical parameters such as microstructure, dislocation density, stresses, and texture [1-11]. To ensure their safe and reliable operation, the fabrication of CANDU pressure tubes involves several steps, including extrusion at ~850°C, air cooling, cold drawing to achieve 30% plastic deformation, and autoclaving for 24 hours at 400°C [12], where the tube attains its final mechanical properties and a protective layer against corrosion on both inner and outer surfaces. At the end of the cold drawing process, the

microstructure of the pressure tube comprises approximately 90% hcp α-Zr (with Nb content <1%) and ~10% metastable bcc β-Zr (with 20% Nb) [16, 17]. During the subsequent autoclaving process, β-Zr partially decomposes and transforms into enriched β-Zr and ωZr [18,19], which impacts on the tube mechanical properties. The kinetics of such decomposition depends on the morphology and microstructural state of the minority β-Zr phase.

The Atomic Energy Commission of Argentina (CNEA) has developed an alternative method for cold shaping of the tubes, where cold drawing is replaced by cold rolling using a pilgering machine to achieve the final diameter and wall thickness of the tube [20]. The process involves a series of rolling passes that reduce the outer diameter and thickness of the tube, with the deformation in both radial and hoop directions being controlled by the shape of the rolling tool.

Control and monitoring of the metallurgical parameters and fabrication process are crucial to meet the required standards for safe and reliable operation. Texture is a critical factor due to its impact in the material mechanical properties [13], and on degradation mechanisms such as delayed hydride cracking [2] and irradiation-assisted creep [55], which dictate the tube´s service life. The extrusion process results in a strong crystallographic texture [12-15] that is only slightly altered during the cold drawing and final autoclaving treatment. Yet, residual stresses develop during the cold working stage, and their magnitude and angular dependence impact on tube performance and in subsequent processing stages. Such stresses manifest over different length scales: whilst macroscopic (Type I) stresses affect the tube mechanical properties and their relaxation may introduce dimensional changes [22], microscopic (Type II) stresses between grains affect microstructural evolution during posterior autoclaving treatments [21].

The objective of this work is to provide sound experimental data on the changes occurring on the crystallographic texture and intergranular stresses of Zr2.5Nb pressure tube material during the later stages of the manufacturing process, not only for the majority αZr phase but also for the minority βZr and ωZr phases. This information provides an insight into the impact of interganular stress on the actual microscopic processes that lead to the decomposition of the metastable βZr phase during autoclaving. For this purpose, we produced small specimens from a pressure tube after extrusion, after cold rolling, and after autoclaving; and measure them using synchrotron X-ray diffraction.

Microscopic residual stresses appear due to mechanical incompatibility between crystalline grains of different phases, or between differently oriented grains of the same phase. Both cases lead to residual stresses that depend on grain orientation, and are therefore dictated by the orientation distribution function (ODF) of the crystallites composing the material [56]. These microscopic, orientation-dependent residual stresses (ODRS) can be quantified by different experimental methods, including X-ray or neutron diffraction. The ODRS is a specific case of the more general stress orientation distribution function (SODF), corresponding to the situation when no external stresses are present.

Most techniques used to determine the ODF and the SODF rely on measuring two types of pole figures: the conventional pole figures of intensity, together with pole figures of lattice strain. The ODF is obtained by applying well-established methods commonly referred to a Quantitative

Texture Analysis (QTA) [56]. SODF studies are much more time-consuming and less common. The function describing the SODF is obtained through a deconvolution method that combines the information provided by both types of pole figures. The deconvolution method is similar to QTA, but while in QTA a unique parameter is associated to each grain orientation (its volume fraction), in the case of SODF, six components are needed to define the state of strain/stress of a grain (the six components of the strain/stress tensor). Therefore, six different distribution functions must be determined. Several deconvolution methods have been proposed in the literature to obtain SODF, and its equivalent version in strain (lattice strain distribution function LSDF) [23-33]. These methods all assume that the different components of the SODF and/or LSDF can be expanded in Fourier series, where the Fourier coefficients of the expansion are used as fitting parameters in a least square method, where an analytical expression of the strain pole figures is compared to the experimental ones.

An alternative method to study the orientation dependence of the stresses is through the study of smaller volumes of material, by using a highly collimated synchrotron X-Rays. In this method, Laue spots produced by a small number of grains are indexed and their change in shape and position are followed as the gauge volume is translated in XYZ over the sample. A detailed 3D map of the strain field can be then constructed. Compared to the deconvolution method, this technique is direct and has the advantage of revealing the strain field inside grains. However, in order to obtain statistical sound data on the dependence of the strain/stress with grain orientation, long experimental times are needed [34]

In the present work, the ODF and SODF were determined for the Zr2.5Nb material in three processing conditions (extruded, cold rolled and after autoclaving) by the deconvolution method. On the experimental side, conventional and strain pole figures were measured in HE-XRD experiments performed at the Advanced Photon Source in Argonne National Laboratory. Section 2 describes the samples and experimental arrangement used in the experiments, as well as data processing details. Section 3 outlines the methodology and introduces the main expressions used to obtain the lattice strain distribution function (LSDF) and stress orientation distribution function (SODF) from the measured pole figures, whilst the details are described in an Appendix. The results are summarized in Section 4, both for the changes in the crystallographic texture of the phases and the evolution of intergranular strain/stress during the process. In the discussion of Section 5, the implication of the main outcomes of the work is discussed and a mechanistic explanation is given for the evolution of texture of the minority phases. Finally, Section 6 outlines the main conclusions of the present work.

2. Experimental details

Zr2.5Nb tubes were provided by Wah Chang Corp in the extruded condition. To study the effect of the cold rolling process and subsequent annealing on the development of intergranular stresses on Zr2.5Nb pressure tubes, coupons of parallelepiped rectangular shape were extracted on tubes in the following conditions: extruded (before cold rolling), at the end of a pilger type cold rolling process up to a total deformation of ~30% and after autoclaving at 400ºC for 24hrs. These coupons were machined to cylindrical shape with 3mm diameter and

4mm length, and then polished using polishing paper maintaining in all cases the longitudinal direction of the cylinder parallel to the hoop direction of the tubes.

Kapoor et al. found that cold-worked pressure tubes have compressive residual stress along both the hoop and axial directions, ranging from 50 to 150 MPa [35]. However, these macroscopic stresses are expected to relax to several tens of MPa during the autoclaving process. In the present case, the stress relaxation is expected to occur during the mechanical cutting of the tube to extract coupons and reduce them to the final sample geometry. Although the macrostresses from the rolling process are expected to relax during coupon cutting, some intergranular and intra-granular stresses resulting from internal defects of the grains may still exist after this sample preparation process.

In order to assess these residual stresses, high-energy X-ray diffraction experiments (at 80 keV) were carried out at the 1-1D line of the Advanced Photon Source synchrotron located at Argonne National Laboratory in the United States [36]. A scheme of the experimental setup is presented in Figure 1(a). The cylindrical sample is placed in a rotating stage with its longitudinal direction (hoop direction of the tube) in the vertical direction. The monochromatic X-Ray beam (λ=0.15Å) goes through the sample producing diffraction cones that are collected by a 2D high speed sensitive screen placed at ~2035mm behind the sample. The direct beam is blocked and images similar to the one shown in the figure are collected, where Debye rings of the different diffracting planes of αZr are clearly observed. The X-ray beam was collimated to a lateral section of 200μm x 200 μm that illuminated the center of the cylinder. The X-Ray detector has a sensitive dimension of 410mm x 410mm with a pixel dimension of 0.2mm x 0.2mm. The exposure time was set to 0.1s to avoid saturation of the detector. The sample to detector distance was chosen to have a large number of diffraction rings (more than 10 complete rings) whilst keeping an angular resolution in the radial direction of the detector plate good enough to perform strain analysis (~100με).

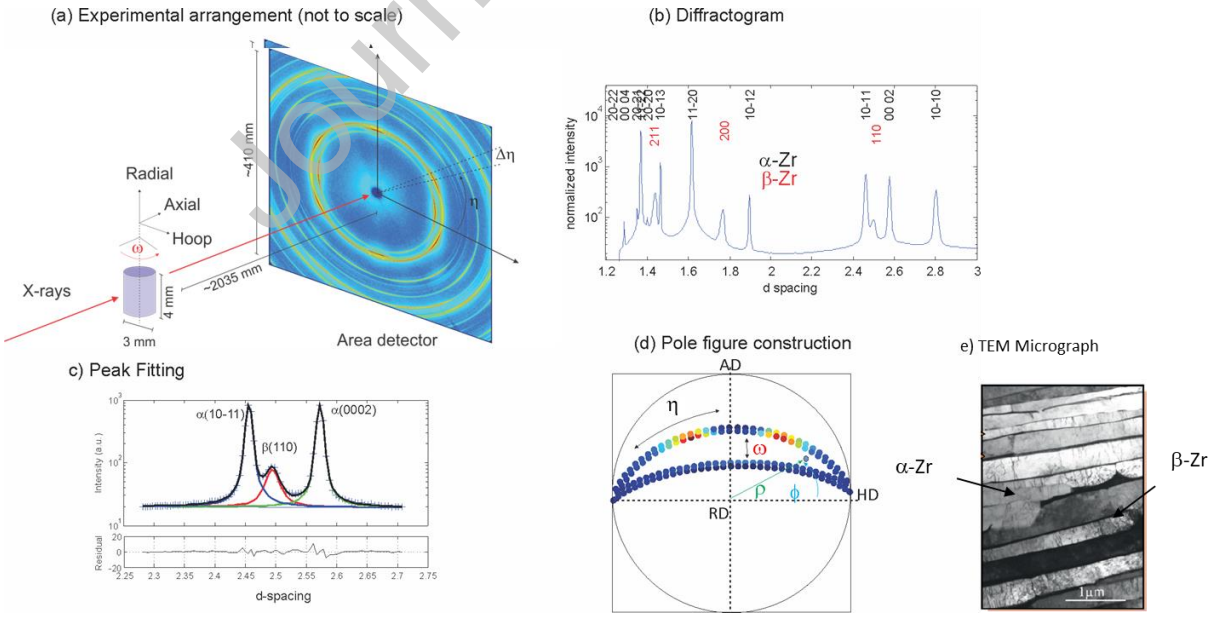

Figure 1: a) Experimental setup in transmission geometry, where the sample is rotated along the vertical direction and the Debye rings are collected by an area detector; b)

diffractogram I vs d-spacing generated from averaging over a "pizza" section of the area detector, peaks corresponding to αZr and the minority phase βZr are indexed; c) fitting procedure, each peak is plotted with different color; d) stereographic projection in a pole figure plot of the area of the peak for scattering vectors corresponding to the different points of the Debye ring and for 2 sample rotation angles; e) TEM micrograph where grains of αZr and βZr are observed as elongated intercalated layers

The samples were rotated around the vertical direction (hoop direction of the tube) from -90º to 90º with 5º step (ω-rotation) and images were recorded. A ceria sample was used to calibrate the working wavelength and the sample-to-detector distance. Correction and data processing of the images have been explained in detail elsewhere [37-39], for that reason only the basic procedure involved in the process of generalized pole figure construction will be described. The process involves dividing each image into "pizza" slices with a width of $\Delta\eta=5°$, as depicted in Figure 1(a). These slices are utilized to construct diffractograms of intensity vs. *d*-spacing, where the intensity is averaged over $\Delta\eta$ and the radius *r* is transformed into *d*-spacing, as illustrated in Figure 1(b).

The process of constructing generalized pole figures is straightforward. From geometric considerations, a direct relation exists between the pair of angles (η,ω) and a point in the pole figure plot. As shown in Figure 1(d), scanning along the Debye ring (η from 0 to 360º) draws two lines on the pole figure plot. Similarly, the rotation angle ω alters the position of these lines. Generalized pole figures can be constructed by plotting various peak parameters. Conventional pole figures for quantitative texture analysis are particularly constructed by using the area of the peaks. Lattice strain pole figures are constructed by plotting $\varepsilon=(d-d_o)/d_o \cdot 10^6$ where ε is the micro-strain, *d* is the fitted *d*-spacing, and d_o is the stress-free *d*-spacing of the same peak. Note that in Figure 1(d), the following convention is used to identify the sample reference system: the radial direction (RD) is at the center, the hoop direction (HD) is to the right, and the axial direction (AD) is to the top. Instead of working with angles (η,ω), it is convenient to define two pairs of angles (ρ,ϕ) to identify each point in the pole figure. Angle ρ ranges from 0 to 90º and represents the angle formed by the scattering vector with the RD, while ϕ is the angle between the scattering vector and the HD in the RD-HD plane. For instance, the RD is represented by (0, ϕ) with ϕ taking any value, the AD is (90º,90º), while the HD is (90º,0).

For each image, a total of 72 diffractograms were generated, each corresponding to a different η angle. The peaks associated with the observed phases were then indexed and fitted using a pseudo-Voigt function with customized MATLAB software. Figure 1(c) presents an example where three peaks (α(10-11), β(110), and α(0002)) were simultaneously fitted. The fitting parameters of the peaks, such as maximum intensity, *d*-spacing, full width at half maximum (FWHM), and shape factor, were recorded for all peaks, as well as for the azimuthal angle η and vertical sample rotation angle ω. Lastly, Figure 1(d) presents in the stereographic projection of a pole figure the location of the scattering vector corresponding to each section of a Debye ring. Figure 1(e) displays a TEM micrograph of the extruded sample taken from Ref[39] where both αZr and βZr phases appear as elongated grains intercalated along the axial direction of the tube.

It is important to note that the use of a wide-angle detector and high-energy X-rays enabled the recording of full Debye rings for a wide range of lattice *d*-spacings. Additionally, sample rotation allowed for full coverage of pole figures for a vast number of diffraction peaks. Since the diffracted beam passes through the same amount of material for all angles along the Debye ring and for all sample orientations, no corrections were needed for attenuation. The MTEX toolbox [41] in MATLAB was utilized both to generate the generalized pole figures and to analyze the orientation distribution function (ODF).

3. Deconvolution method for the evaluation of the stress/strain orientation distribution functions

The determination of the lattice strain (LSDF) and stress distribution function (SODF) through strain pole figure (SPF) inversion has been addressed by several authors [23-33]. However, these methods rely on certain assumptions. Firstly, all grains with the same orientation are assumed to have the same strain tensor. Secondly, the experimental strain $\varepsilon_{hkl}(\rho,\phi)$ corresponding to angular position (ρ,ϕ) in the pole figure *(hkl)* is estimated as a weighted average of the strain of all grains under diffraction, with the weighting factor being the volume fraction of the contributing grains. Finally, the dependence of the strain/stress tensor on grain orientation is expanded as a Fourier series, reducing the problem to obtaining the Fourier coefficients of this series.

The second assumption can be mathematically expressed as:

$$\varepsilon_{hkl}(\rho,\phi) = \frac{d_{hkl}(\rho,\phi)-d_0}{d_0} = \int_{g_\perp} \varepsilon_g(\rho,\phi) f(g) dg \,/ \left(\int_{g_\perp} f(g).dg\right) \quad (1)$$

where $\varepsilon_g(\rho,\phi)$ is the effective strain contribution along direction (ρ,ϕ) of those grains with orientation g, and integration is done over all orientations $g_\perp$ for which plane normal *(hkl)* or *–(hkl)* point along direction (ρ,ϕ) in the sample reference system. In turn, $\varepsilon_g(\rho,\phi)$ can be expressed in terms of the components of the strain tensor ε_{ij}^{g} using the direction cosines $\propto_i$:

$$\varepsilon_g(\rho,\phi) = \sum_{ij} \propto_i \propto_j \varepsilon_{ij}^{g} = \varepsilon_{11}^{g}.\cos(\phi)^2.\sin(\rho)^2 + \varepsilon_{22}^{g}.\sin(\phi)^2.\sin(\rho)^2 + \varepsilon_{33}^{g}.\cos(\rho)^2 +$$
$$\varepsilon_{12}^{g}.\sin(2.\phi).\sin(\rho)^2 + \varepsilon_{23}^{g}.\sin(\phi).\sin(2.\rho) + \varepsilon_{13}^{g}.\cos(\phi).\sin(2.\rho) \quad (2)$$

where summation ij goes from 1 to 3. In this case to be consistent with the definition of angles (ρ,ϕ) given in Figure 1(d) we have 1=AD, 2=HD and 3=RD.

Strain tensor ε_{ij}^{g} and stress tensor σ_{ij}^{g} are related by Hooke's law

$$\sigma_{ij}^{g} = \sum_{k,l=1,3} c_{ijkl}\varepsilon_{kl}^{g} \quad (3)$$

where the fourth rank tensor c_{ijkl} is the single crystal elastic stiffness.

Both strain tensor ε^{g} and stress tensor σ^{g} are function of the grain orientation g and as such, each component of the tensor must adhere to the symmetry properties of the crystal space group: $\varepsilon_{ij}^{g} = \varepsilon_{ij}^{g_o g}$, where g_o represents any rotation within the crystal space group. As such, they can be expended in Fourier series of symmetrized generalized spherical harmonics.

By substituting Eq. (2) into Eq. (1), it is possible to obtain a relationship between the experimentally determined strain pole figure (SPF) and the lattice strain orientation distribution function (LSDF). Similarly, by replacing Eq. (3) into Eq. (2) and then into Eq. (1), an expression linking the SPF with the lattice stress (SODF) can be obtained. To determine either the LSDF or the SODF, the method involves expanding ε_{ij}^{g}, σ_{ij}^{g}, c_{ijkl} and the ODF $f(g)$ as Fourier series of generalized spherical harmonics. Then, analytical solutions for the integrals along $g_{\perp}$ in Eq. (1) are then obtained, leading to a linear expression of the SPF data in terms of the Fourier coefficients of the strain/stress tensor. Finally, the Fourier coefficients are determined using a least-squares minimization method.

In the present work, the approach introduced by Wang et al. in Ref[23] was adopted but employing the symmetrized generalized spherical harmonics described in Bunges's book [40] as expansion functions.. A detailed derivation of the SPF expression in terms of these functions is provided in APPENDIX I. The method was implemented in MATLAB, utilizing various functions from the MTEX library [43]. Some specific conditions are assumed when applying the proposed inversion method to the cases of αZr , βZr or ωZr, which are explained in more detail in Section 4.3.

4. Results

4.1 Crystallographic texture

4.1.1 αZr phase

Figure 2(a) displays the recalculated pole figures for the first four αZr peaks obtained from the cold rolled sample. Similar pole figures were observed for the cold worked and after autoclaving. Figures 2(b) to (d) present the Phi1=0° section of the ODF for the extruded sample, cold rolled and annealed samples, respectively, in which the most prominent texture components appear. These textures are characterized by the presence of a strong fiber texture with the <11-20> direction aligned with the AD. This fiber is responsible for the high intensity of the ODF observed along Phi; for Phi1=Phi2=0°. The *c*-axis of the hexagons concentrate in the RD-HD plane with the strongest intensity for those grains oriented with their *c*-axis aligned with the HD (Phi=90°) and a smooth decrease as the grains rotates toward the RD (Phi=0°). As seen in the ODF cuts, after cold rolling, there is a small increase of the m_{Hoop} orientation, and a reduction of intensity for Phi<40.

Previous works have shown the importance of intermediate grain orientations near m_{Tilted} (Phi2=0°, Phi~70°) in which there is a higher probability of hydride precipitation upon water corrosion of pressure tubes [37,39], an aspect that will be revisited on the light of the present experiments.

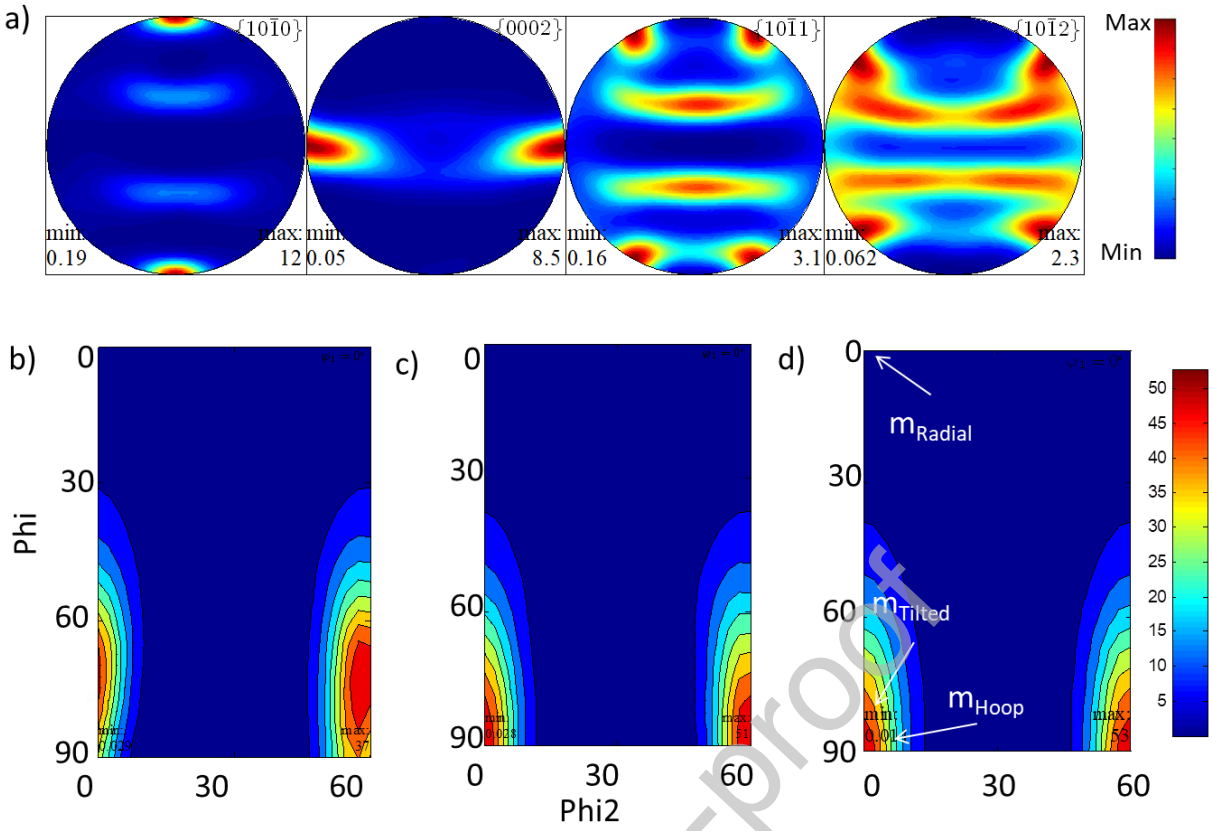

Figure 2: Texture of αZr. Top: a) recalculated pole figures for the extruded sample. Bottom: Phi1=0 cut of the ODF for the (b) extruded, (c) cold rolled, and (d) after autoclaving samples, respectively. In both cases, the color scales are in multiples of times random (MTR).

4.1.2 Minority phases: βZr and ωZr

Besides the major αZr phase, the experimental diffractograms revealed the presence of cubic βZr in the samples, and the additional hexagonal ωZr phase in the sample after autoclaving. The ωZr phase result from the decomposition of the metastable βZr phase at 400ºC, the autoclaving temperature [18].

The α-β phase transformation in Zr is a well-known phenomenon that follows Burgers Orientation Relationship (BOR) between the crystallographic lattices, namely that α(0001)//β(110) and α<11-20>//β<111> [16,17,44,45]. According to Ref [46-48], ωZr forms as precipitates in βZr also following a precise orientation relationship: β(111)//ω(0001) and β<-110)>//ω<11-20>. In the presentation and analysis of the results of the crystallographic texture of minority phases, the experimental pole figures and ODFs measured for the daughter phase will be compared with theoretical results obtained by applying the corresponding orientation relationship reported in the literature to the experimental ODFs of the parent phase.

Four diffraction peaks were successfully resolved of the βZr phase in the extruded and cold rolled samples, namely (110), (200), (211), and the higher order (220) peak. The ODF was

evaluated using the first three peaks. Figure 3(a) presents recalculated pole figures for the extruded sample of those three peaks, as well as a fourth pole figure associated with the (111) plane. Similar pole figures, not shown here, were obtained for the cold-rolled sample. No recalculated pole figures could be produced for the sample after autoclaving, because it displayed only a weak (200) peak from the βZr phase, whilst the (110) and (211) peaks were so weak that they could not be resolved from the intense αZr peaks, hence preventing the evaluation of the ODF. As mentioned, such reduction in intensity is due to the decomposition of the βZr during autoclaving.

Figure 3(b) presents the corresponding theoretical pole figures evaluated by applying the Burger's orientation relationship to the αZr ODF presented in Figure 2. Two assumptions are made in such evaluation: (i) all orientation variants are given an equal probability of occurrence, and (ii) all αZr grains have the same probability for transformations, e.g., the number of βZr daughter crystals depend directly on the number of αZr parent crystals of each orientation present on the sample. Comparison of Figures 3(a) and 3(b) reveal that the Burgers orientation relationship successfully reproduces all the observed poles in the βZr texture. However, although the same texture components are present in both the experimental and theoretical pole figures, there are variations in the intensity of the poles. Notably, in Figure 3(a), there is an obvious asymmetry between the top and bottom of the figures, which is less pronounced in Figure 3(b). The origin of these differences indicates failure of either of the two assumptions, and needs further investigation.

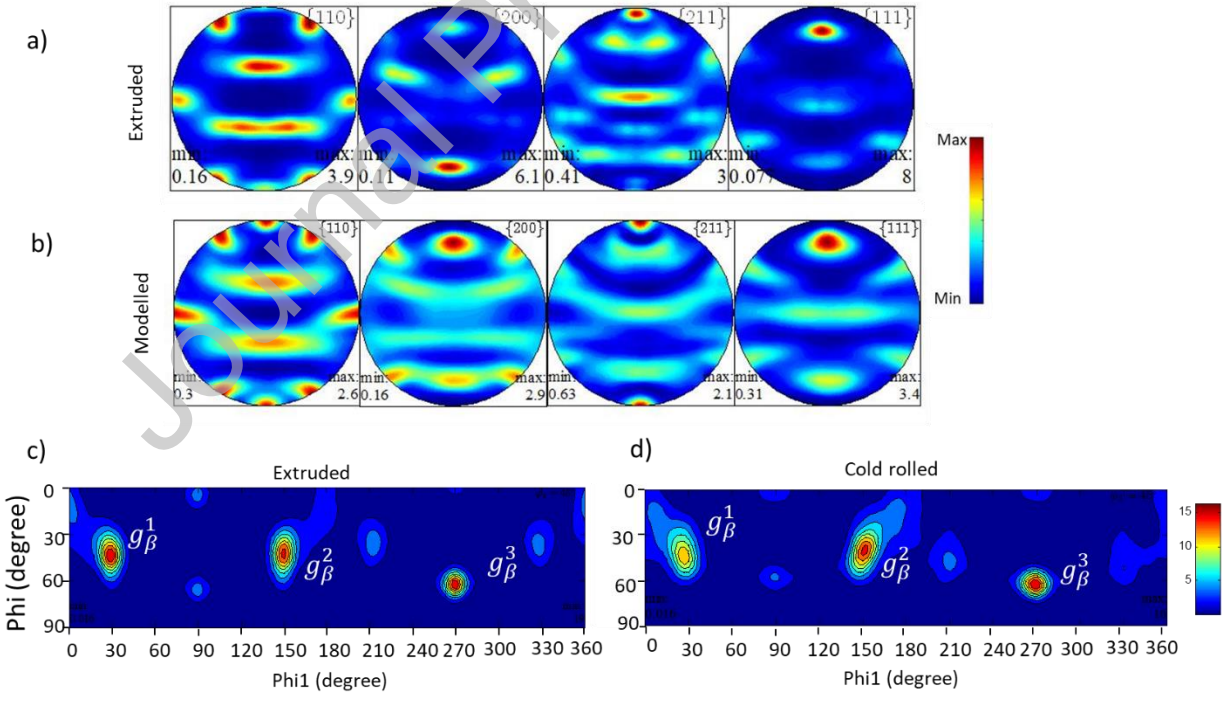

Figure 3: Texture of βZr. Top: (a) Reconstructed pole figures of extruded sample. Center (b) Theoretical pole figures, evaluated by applying the Burgers Orientation Relationship to the αZr texture of Fig 2. Bottom: Cut of the experimental ODF for Phi2=45 for the (c) extruded and (d) cold rolled samples. Color scales are in MTR.

Figure 3(c) displays the Phi2=45º section of the βZr ODF for the extruded sample, which identifies the three principal texture components. Specifically, components g_β^1 and g_β^2 appear at Phi=45º and Phi1=30º and 150º, respectively, and correspond to the {223}<522> texture orientation, while component g_β^3 appears at Phi=60º and Phi1=270º, and corresponds to the {332}<113> texture orientation. Figure 3(d) shows the corresponding cut of the βZr ODF for the cold rolled sample. No major changes are observed in the texture of the sample, with the main components essentially conserving their location. In the case of the extruded sample, the poles are more concentrated than for the cold rolled sample. These three texture components are enough to explain all the pole structure observed in Figure 3(a).

To assess the impact of autoclaving on the texture of βZr, Figure 4 compares the experimental (200) pole figures registered for the three samples, together with the theoretical (200) pole figure presented in Figure 3(b). Each point in the experimental pole figures corresponds to a measurement, with the color scale in counts, and the white regions indicating orientations with counting below the accepted threshold. As mentioned, no qualitative texture changes appear after cold rolling, only a spread of the poles, which reflects as a drop in the maximum intensity of the pole figure of ~40%. By contrast, the pole structure change completely for the sample after autoclaving: the three intense poles that resulted from the main orientations g_β^1, g_β^2, and g_β^3 have disappeared, and a structure composed by five distinct poles emerges, but with nearly a tenfold decrease in the pole intensities. Comparison with the theoretical pole figure reveals that these orientations were already expected by the Burgers orientation relationship. They are indeed present in the pole figures of the extruded and cold rolled samples, but the intensity of the poles is too low to be distinguished with the overall color scale. This indicates that during autoclaving decomposition of the βZr occurred mainly in grains belonging to the main orientations g_β^1, g_β^2, and g_β^3, and it was much less likely in grains of other orientations.

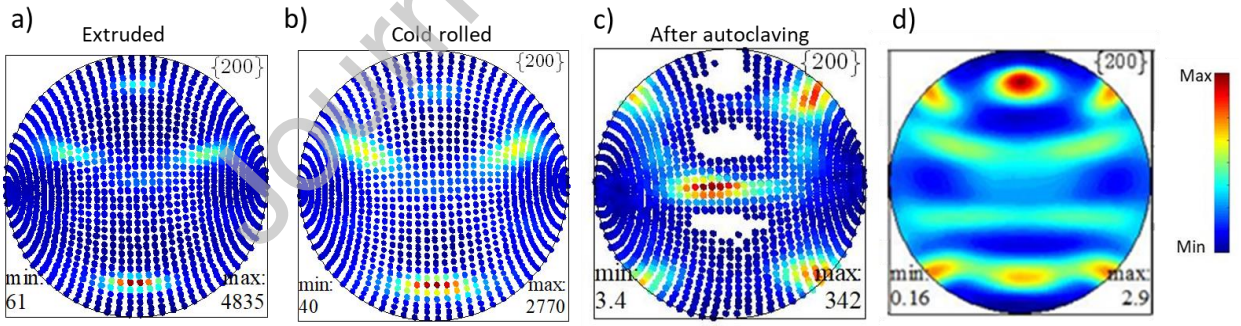

Figure 4: Comparison of the experimental βZr. (200) pole figures (a to c) obtained for the three conditions with (d) the pole figure evaluated by applying the Burgers Orientation Relationship to the αZr texture of Fig 2.

Although it was not possible to produce an ODF of the βZr phase present in the sample after autoclaving, it was indeed possible to produce a detailed ODF for the ωZr phase that resulted from the decomposition. Several distinct peaks of the ωZr phase were clearly resolved, including (0001), (11-21), (20-21), (0002), and (11-22); and the experimental pole figure are presented in Figure 5(a). As before, region in white corresponds to peak intensity below the

threshold. Figure 5(b) shows a cut of the evaluated ODF, for Phi1=90°. The intensity of the ODF outside this section is low, and the texture of ωZr can be represented by a single pole distributed around the orientation (Phi~60°, Phi2=30°, and Phi1=90°). This orientation corresponds to ωZr hexagons with their c-axis shifted 30° from the axial direction of the tube along the radial-axial line, as observed from the (0001) pole figure. Interestingly, although the βZr texture of the extruded and cold-rolled sample exhibits marked asymmetry, the texture of the resultant ωZr phase is symmetric.

Figure 5(c) presents the same section of (b) for a theoretical ODF of ωZr obtained by applying the orientation relationship reported in the literature, ω(0001)//β(111) and ω<11-20>//β<110>, to the βZr texture of Figure 3(d). Again, the evaluation assumed suppositions (i) and (ii) mentioned for the evaluation of the βZr texture, e.g., equal probability for all variants and grain orientations. The main pole observed at Phi=60° in Figure 5(b) is well reproduced, indicating that the orientation relationship between these two phases holds. However, additional poles appear in the estimated ODF that were not observed in the experimental texture (for example the one at Phi=0, Phi2=30°, Phi1=90° in Figure 5(c)). The characteristics of the experimental texture of ωZr could be indeed reproduced, when considering that only the most intense texture components of βZr (g_{β}^{1}, g_{β}^{2}, and g_{β}^{3}in Figure 3) decompose but with a strong variant selection. This finding is in line with the information provided by the (200) βZr pole figure, as discussed in relation to Figure 4, which indicated that grains with these orientations are more likely to decompose into ωZr. Thus, these results reveal that the kinetics of βZr decomposition does indeed depend on the orientation of the parent βZr grains.

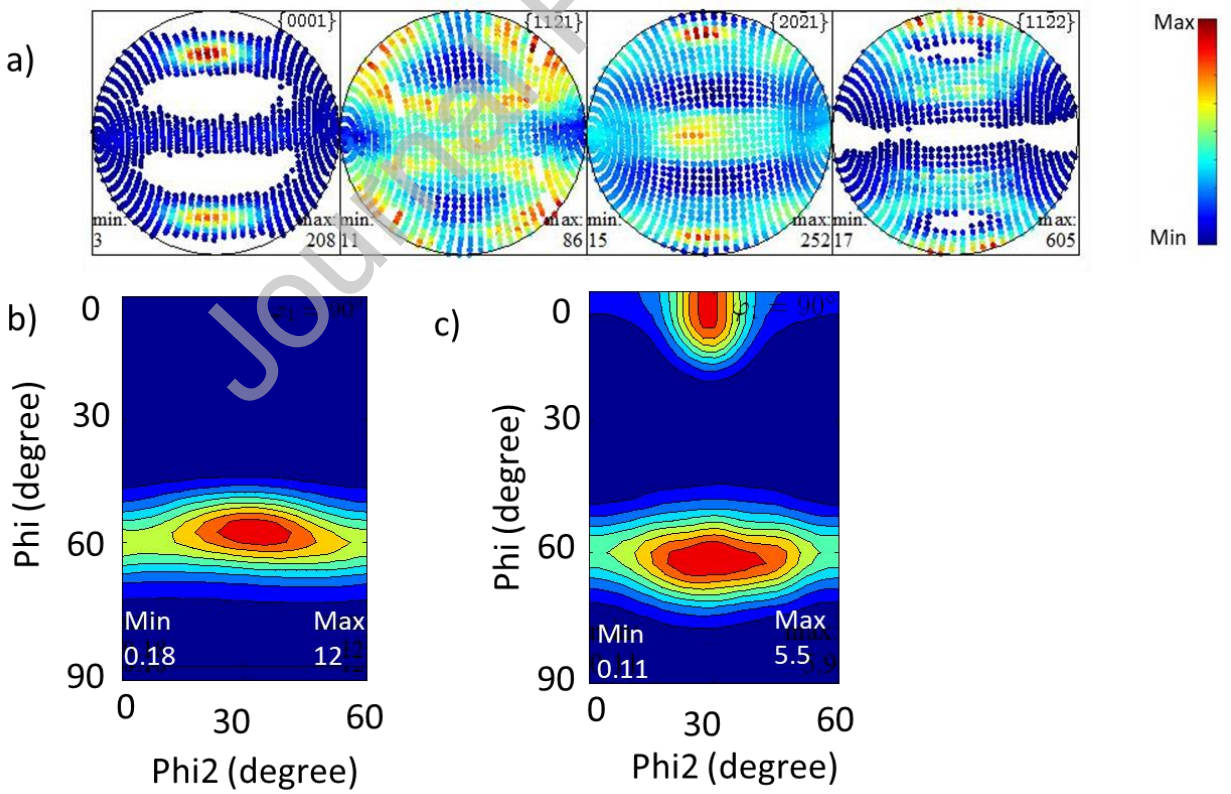

Figure 5: Texture of ωZr in sample after autoclaving. Top: a) Experimental pole figures, with scale in counts; Bottom: Comparison of the Phi1=90º section of (b) the experimental ODF, with (c) the theoretical ODF , evaluated by applying the orientation relationship ω(0001)//β(111) and ω<11-20>//β<110>, to the βZr texture of Fig 3(d). Both ODF scales are in MTR.

4.2-Strain pole Figures

This section presents the experimental strain pole figures for αZr for the three processing conditions, for βZr for the extruded and cold rolled samples, and for ωZr for the sample after autoclaving. As described in Section 2, stress free values of *d*-spacing for the corresponding diffraction peaks are required to construct the strain pole figures. As those values are no directly accessible for Zr2.5Nb material, composed by a major Zr-based α phase and the minority phases of varying compositions, the assumptions and the values adopted for each phase are presented below. The basic assumption in all cases is that an unstressed unit cell exists for each phase, and the unstressed *d*-spacings used to produce the strain pole figures are evaluated from the lattice parameters of such unit cell.

4.3.1 αZr phase

For αZr the lattice parameters of the unstressed cell for each processing condition were evaluated by least-squares fitting of as many unstressed *d*-spacings as experimentally accessible. For this purpose, the unstressed *d*-spacing of the *(hkl)* family was firstly approximated by the weighted average of the d_{hkl}´s measured at all orientation explored in the corresponding pole figure. The weighting was based on the area of the peaks for each point, which allowed prioritizing grain orientations that had a greater influence on the orientation distribution function (ODF). The weighted average of the interplanar distances and the values of lattice parameters *a* and *c* of the stress free unit cell are presented in Table 1.

Processing Condition	10-10	0002	10-11	10-12	11-20	10-13	11-22	20-20	20-21	0004	*a*	*c*
Extruded	2.7984	2.5737	2.4589	1.8949	1.6163	1.4630	1.3686	1.3996	1.3505	1.2869	3.2319	5.1477
Cold rolled	2.7982	2.5744	2.4588	1.8949	1.6162	1.4631	1.3686	1.3991	1.3504	1.2872	3.2315	5.1489
After autoclaving	2.7983	2.5739	2.4590	1.8950	1.6162	1.4630	1.3687	1.3991	1.3504	1.2871	3.2317	5.1482

Table 1: Stress free d-spacing estimated for the different diffraction peaks of αZr. In the last two columns we present the estimated stress free lattice parameters

Compared to the lattice parameters reported for pure Zr (*a*=3.2321 Å and *c*=5.1477 Å) [49], our observations for the extruded and after autoclaving samples show differences of less than 100 με, which is within the experimental uncertainty. The cold-rolled sample exhibits a very small extension of the *c*-axis by 200 με and a contraction of the *a* length by -200 με, both just above the experimental uncertainty. However, in all three cases, there is a negative net volume change compared to pure Zr, which suggests a real very small changes in lattice parameters,

which could attributed to the influence of small amount of Nb in solid solution, which has a slightly smaller atomic radius than Zr.

The first 4 columns at the left of Figure 6 displays the experimental strain pole figures for the three samples, with eight of the ten diffraction peaks shown. The (20-20) and (0004) peaks were excluded since they are similar to their lower-order reflections (10-10) and (0002), respectively. However, some experimental points were filtered out due to high strain error during peak fitting, resulting in missing points that appear as vertical white lines in all the pole figures and as white regions in the (0002) pole figures close to the AD. To be accepted, a threshold error value of 300 με was imposed. The color scale is different for each sample, but is common to all the pole figures. The extruded material's strain ranges from -1500 to 500 με, while the cold rolled sample's strain widens to values between -4500 to 1500 με. Finally, the annealed material exhibits a significant relaxation of stresses, and strain values fall again to -1200 and 600 με. The complex internal structure of the pole figures varies from plane to plane, highlighting the importance of intergranular stresses and their dependence on grain orientation.

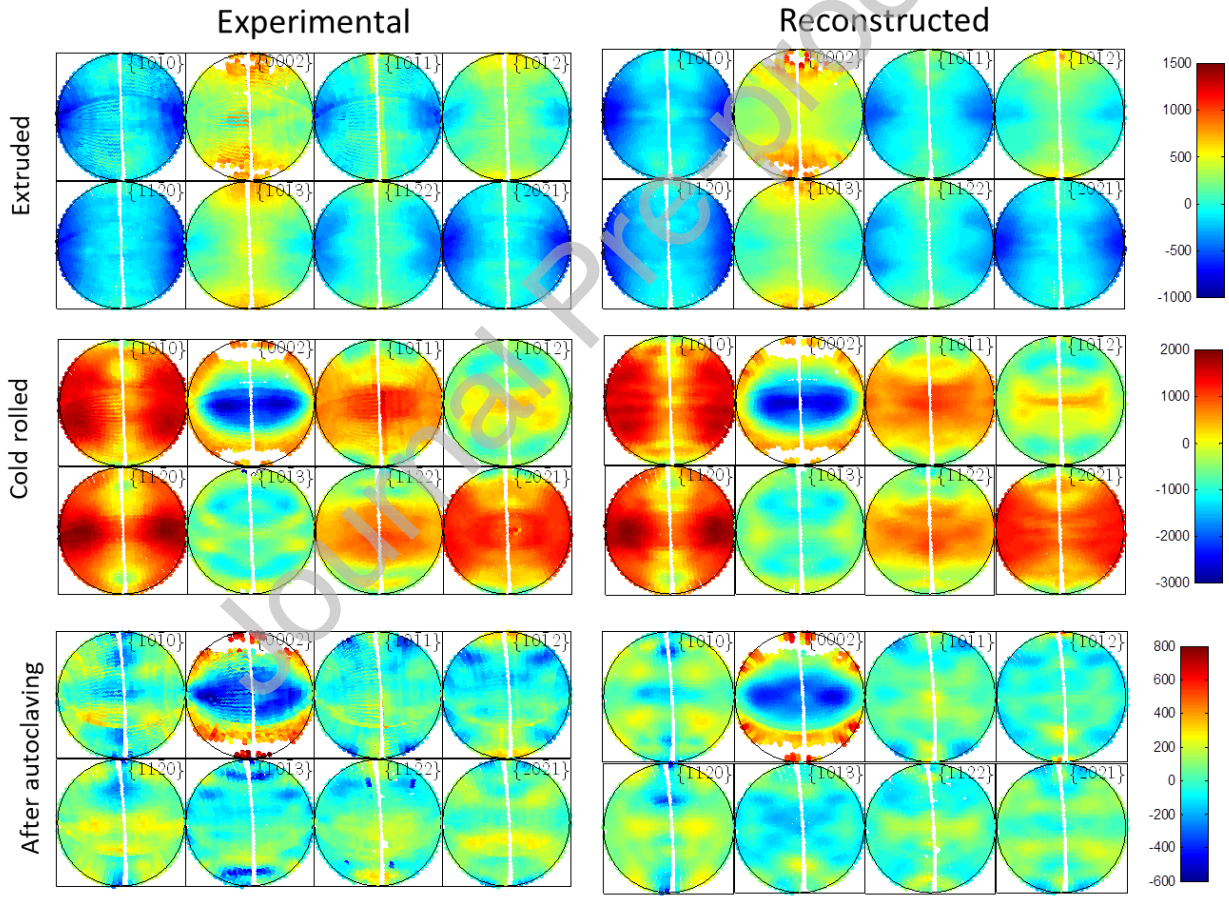

Figure 6: Comparison between the experimental strain pole figures of αZr (4 first columns to the left left) and the model after fitting (columns 5 to 8) for the three processing conditions. The scales are in με.

4.3.2 Minority phases: βZr and ωZr

For βZr, a change in the lattice spacing is expected due to variations in the amount of Nb in solid solution within the cubic lattice. A linear relation exists between lattice parameter of β_{enr} and the Nb content [51], hence allowing to indirectly measure the Nb content from the measured lattice spacing. As done for αZr, Table 2 presents a summary of the averaged values of *d*-spacing of the 4 diffraction peaks, together with the refined lattice parameter *a*, and the estimated Nb content in atomic percent. As expected, the average lattice parameter for the three samples falls between the pure βZr lattice parameter of 3.5882 Å [50] and the pure βNb lattice parameter of 3.30 Å [49]. Values of 20at%, 23at% and 50at% are obtained for the extruded, cold rolled, and after autoclaving samples, respectively. The 3% difference in the total amount of Nb between the extruded and cold rolled sample could be due to differences in the extrusion temperature and cooling conditions of the region of the material where the sample were taken.

In the sample after autoclaving, the decomposition of the original βZr phase produced the ωZr and a new βZr phase enriched in Nb content (β_{enr}) [18]. For this sample only the (200) peak was resolvable, and the average *d*-spacing of 1.725 Å reveals a β_{enr} phase containing ~50% Nb, consistent with the findings of Kim et al. [51].

For simplicity, the experimental strain pole figures were constructed considering a stress free lattice parameter for pure βZr (3.5882 Å). This introduces an overall shift for grains of all orientations, associated to the average Nb content of the sample. Figure 7 shows the experimental βZr strain pole figures for the extruded and cold-rolled samples (first 4 columns in the left). As it will be discussed in section 4.3, the LSDF inversion method applied here allows a detailed insight on how Nb distributes among the βZr grains of different orientations.

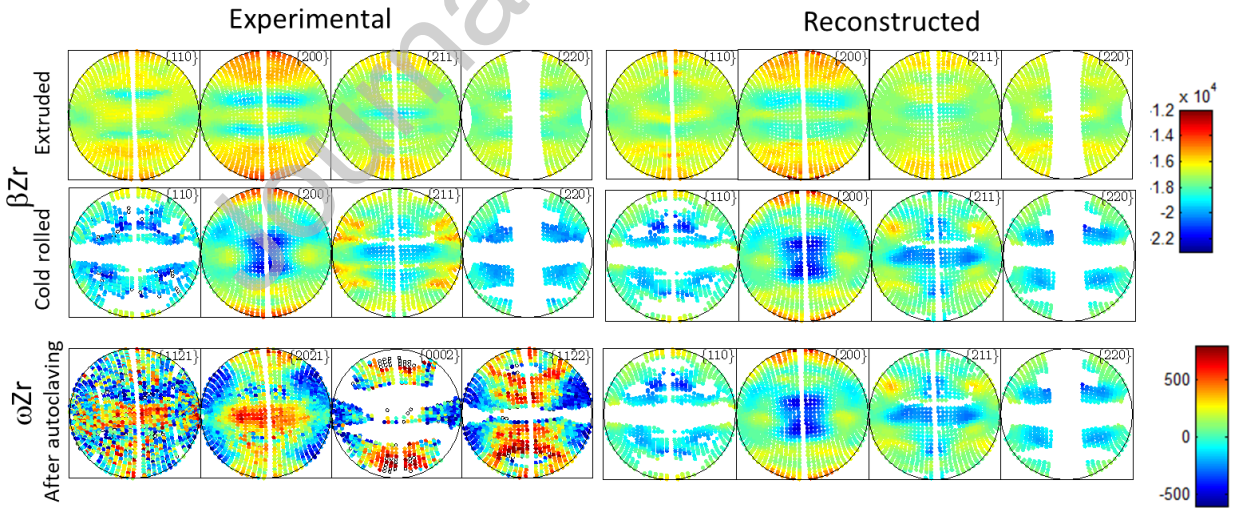

Figure 7: Comparison between the experimental strain pole figures of βZr (four first columns) and the model after fitting (columns 5 to 8) for the extruded and cold rolled samples. At the bottom the same comparison is presented for ωZr for the heat treated sample. The scales are in με.

Processing Condition	110	200	211	220	*a*	Nb at.%
Extruded	2.4943	1.7637	1.4397	1.2466	3.5268	20
Cold rolled	2.4889	1.7618	1.4394	1.2447	3.5224	23
After autoclaving		1.725			3.45	50

Table 2: Stress free d-spacing (Å) estimated for the different diffraction peaks of βZr. In the last column we present the estimated stress free lattice parameter.

As for αZr, in the case of ωZr, the strain pole figures were constructed from the lattice parameters of the unstressed unit cell. Table 3 summarizes the average *d*-spacing for the different diffraction peaks. Compared to the values reported by other authors in Ref[52] (*a*=5.040, *c*=3.125), there a small contraction of the lattice in the basal plane. The resulting strain pole figures for ωZr is also presented in Figure 7. By contrast to βZr, the variation of strain with sample orientation for ωZr is relatively small in the sample after autoclaving, and is in the same order of magnitude of the strains measured for αZr.

ProcessingCondition	11-21	20-21	0002	11-22	*a*	*c*
After autoclaving	1.96	1.787	1.5625	1.327	5.033	3.125

Table 3: Average values of d-spacing (Å) for the different diffraction peaks of ωZr. In the last column we present the estimated lattice parameter.

4.3 LSDF and SODF

As mentioned in Section 3, additional assumptions are necessary to improve the robustness of the fitting process. These assumptions differ between the phases, and may allow fixing some of the components of the macroscopic strain or stress tensors. Here, it was assumed that no macroscopic stresses occur within the samples due to the small size of the coupons and the careful process used to produce them. This implies that the macro-stresses calculated considering all of the phases must be null. As the volume fraction of αZr is around 95%, it is a good approximation to assume that the macro-stress for this phase is almost negligible. This assumption is not valid for the minority phases, βZr, and ωZr, hence no extra conditions were imposed during the minimization procedure.

Table 4 lists the cutoff values Lmax of the strain (LSDF) and stress (SDF) Fourier expansion (these quantities are defined in Appendix I), the number of Fourier coefficients used for each strain component, the number of total fitting variables, and the number of experimental points involved in the inversion process, and the stiffness tensor constants adopted for each phase. The reason for the reduction in the cut-off value for ωZr is due to the limited number of pole figures available for this phase, which are also more noisy compared to those obtained for αZr and βZr.

Phase	Lmax	No of coeff.	No fitting variables	Exper points	Single crystal stiffness (GPa) and Reference
αZr	6	40	240	~19000	$c_{1111}=c_{2222}=143.4$, $c_{3333}=164.8$, $c_{2323}=c_{1313}=32$, $c_{1212}=35.3$ $c_{1122}=72.8$, $c_{1133}=65.3$ Ref[21].
βZr	6	23	138	~8800	$c_{1111}=145.9$, $c_{1122}=117.4$, $c_{1212}=29.8$, Ref[16].
ωZr	4	15	90	~7800	$c_{1111}=167$, $c_{2323}=33.7$, $c_{1122}=69.8$, $c_{3333}=198.7$, $c_{1133}=47.4$, $c_{1212}=48.6$, Ref[53].

Table 4: Parameters used for the Fourier expansion of strain and stress pole figures

In establishing the optimal value for L_{max} in the series expansion of the strain tensor components, a systematic approach was employed. The dependence of residuals per point was assessed across incremental values of L_{max}. The first instance where residuals fell below a predefined threshold was selected. For αZr, this threshold was set at 100με, while for βZr and ωZr, it was set at 200με. Caution is advised when utilizing L_{max} values exceeding 10, as the LSDF may yield unrealistically high values in regions of the Euler space characterized by a low ODF.

Subsequent to the fitting process, the optimal values of the parameters, along with their respective covariant matrix, are acquired. Then, estimations of errors associated with the strain and stress tensors become attainable. For αZr, the error margin of the reported stress values is maintained below 15 MPa. Similarly, in the case of βZr, the reported strain values for the most prominent texture components exhibit associated errors below 300με.

It must be kept in mind that the LSDF and SDF provide information of the six individual components of the strain and stress tensors, for all possible orientations of the crystallites, regardless of their actual number in the sample. Because of this, even cuts of these distribution functions present an enormous amount of information that is not relevant to understand the effective strain or stress sates of the sample. Hence, for better understanding the results are presented in terms of hydrostatic and deviatoric stress components, specified for the main fiber texture for αZr, and for the main texture components for the minority phases. Additional information from the refined LSOF and SODF is presented in Appendix II

4.4.1 αZr phase

The right columns (5 to 8) of Figure 6 presents the results of fitting the experimental SPF for the three samples analyzed. The color scale used for each sample is the same for both the experimental and calculated data, and the quality of fitting is excellent. Figures A2.1 of Appendix II shows a cut with Phi1=0 of the SODF for the three samples, with discrimination for the six tensor components. In this cut of the ODF the most intense texture components are present. Among the three samples, the shear components AR and AH have the lowest values, particularly in the extruded sample and the sample after autoclaving (see Figures A2.1 to A2.3), where these components are almost negligible. The diagonal components of the stress tensor and the shear component HR vary markedly during cold rolling and relax after heat treatment.

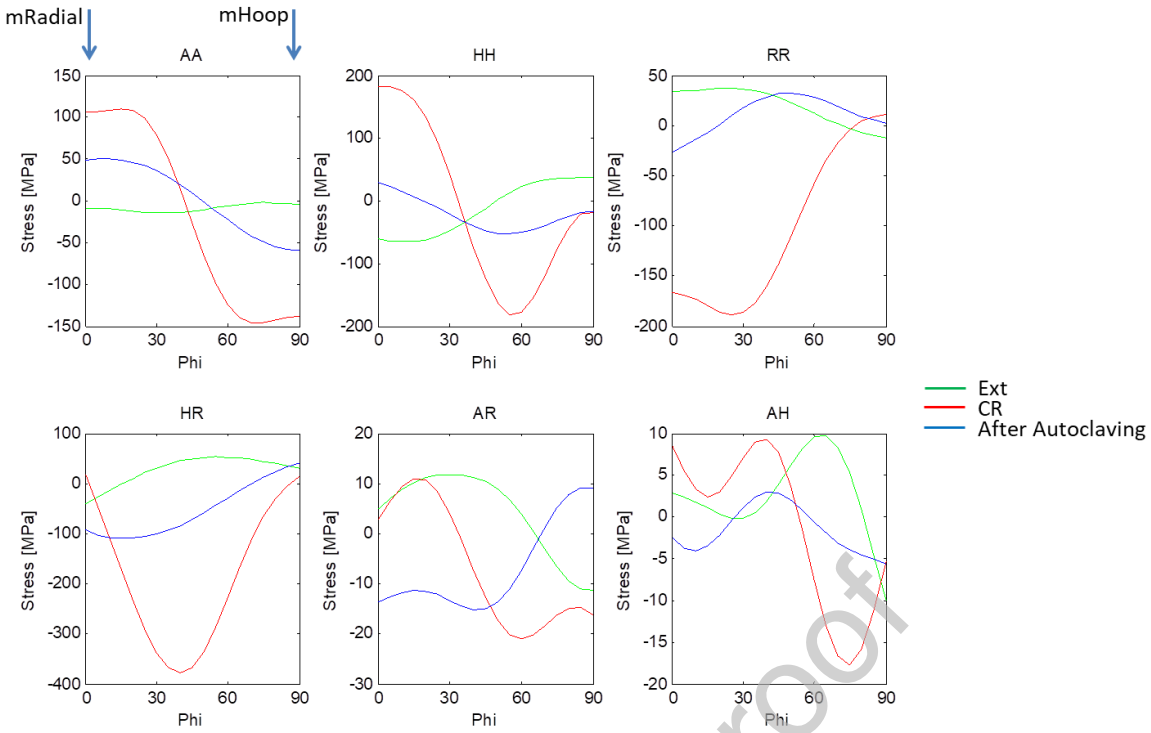

Figure 8: Profiles of the 6 tensor components SODF of αZr along the line Phi1=0, Phi2=0 for the three sample: extruded (green), cold rolled (red) and after autoclaving (blue).

Figure 8 compares the six components of the stress tensor for the line Phi1=Phi2=0, corresponding to the region in the Euler space along the most important texture fiber (as seen in Figure 2). This figure clearly shows the marked effect of cold rolling and the effectiveness of autoclaving in relaxing intergranular stresses. The shear components AR and AH are almost negligible compared to the other components. However, the shear component HR shows values close to zero for Phi=0 (radial) and Phi=90º (hoop) and presents maximum values close to Phi=45º, which are comparable to the three diagonal stress terms. This indicates that the principal stress components differ from the reference axis of the tube. After cold rolling, significant intergranular stresses develop, with values ranging from +200 to -350MPa. Note that we imposed zero macro stress during fitting, so if some grains are under strong stress, there must be other grains (with different orientation) that compensate for it. This condition applies to average over the entire Euler space, not to the reduced set of orientations included in Figure 8. The values estimated for the intergranular stresses are comparable to the residual stresses expected for this type of material after cold deformation [34]. Compared to a yield strength of ~500MPa, these values indicate the importance of intergranular stresses in evaluating the mechanical response of the material.

For the αZr phase, the reconstructed hydrostatic strains can be almost univocally ascribed to internal stresses. Figure 9 compares such hydrostatic stresses for the line of the ODF with Phi1=Phi2=0 for the three processing conditions, identifying the position of the main texture components along this line. Figure 10 shows a graphical representation of the state of strain of the hexagons for three selected grain orientations (a) m_{radial}, b) Phi=45º, and c) m_{hoop}) for the cold-rolled sample. The black hexagons represent the unstrained state, while the red hexagons represent the strained state (to visualize the differences, the strain was multiplied by 50). The

arrows in the figures indicate the direction of the strain or stress along the three principal directions. If an arrow is absent, it signifies low strain or stress. The m_{radial} grains are compressed along the radial direction and tensile strained along both the hoop and axial plane. The grains oriented at Phi=45° are compressed strained along the *c*-axis and compressed along the [10-10] axis, and almost unstrained along the [11-20]. Finally, the m_{hoop} grains (the main texture component) are compressed along the axial direction and tensile strained along the radial direction, while they are almost unstrained along the hoop direction (c-axis of the hexagons).

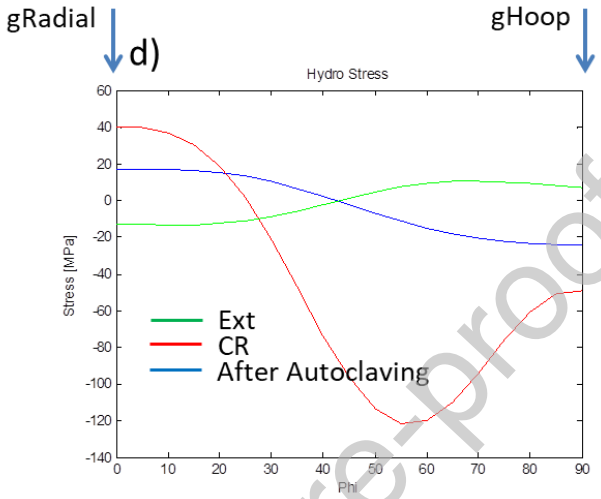

Figure 9: Profiles of the hydrostatic stress of αZr along the line Phi1=0, Phi2=0 for the three sample: extruded (green), cold rolled (red) and after autoclaving (blue).

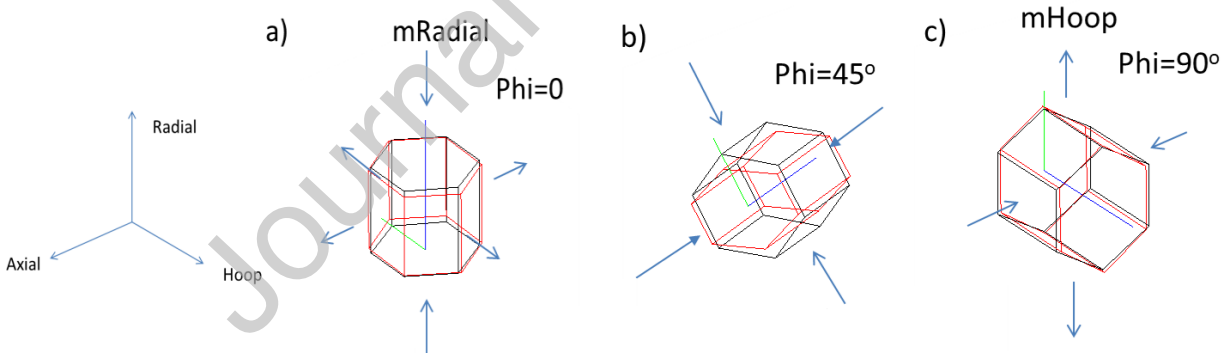

Figure 10: Graphical representation of the state of the αZr hexagonal crystals for three most important/representative orientations of the ODF in the cold rolled sample. The stressed state is represented by red hexagons, while the unstressed state is represented by black ones.

4.3.2 Minority phases: βZr and ωZr

The right columns (5 to 8) of Figure 7 present the results of fitting the experimental SPF of βZr for the extruded and cold rolled samples, showing very good agreement with the experimental data. Figure A3.1 of Appendix 3 presents the six individual components of the LSODF. Figure 11 presents the hydrostatic strain evaluated from the reconstructed strain tensors for both samples. The figure displays the cut Phi2=45°, which contains the main texture components

introduced in Figure 3. To aid the visualization of the results, only those orientations with ODF intensities higher than 20% of the maximum value are presented, whilst less probable orientations appear in white.

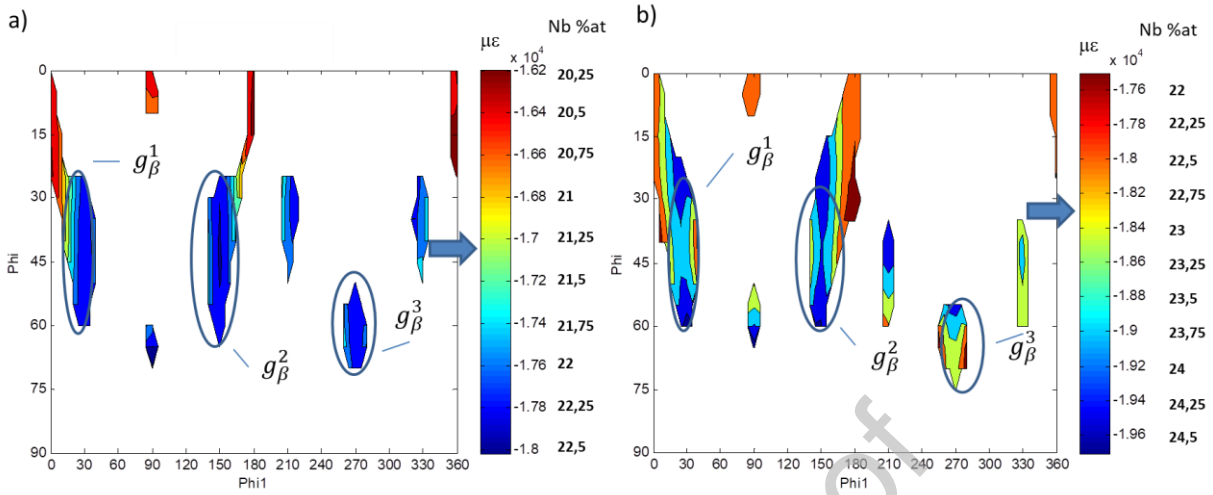

Figure 11: Hydrostatic lattice strain for the main texture components of βZr for (a) extruded, and (b) cold rolled samples. Values evaluated from the recalculated diagonal. The scale also indicates the estimated concentration of Nb in %at. The blue arrows indicate the average value measured for each sample from Table 2.

In both samples hydrostatic strains are in the order of ~10^4 με and vary among the different grain orientations. These high strain values (as referred to pure βZr) correspond mainly to the lattice expansion as a result of the ~20%at Nb content listed in Table 2. Hence, next to the strain scale, a second scale is included to represent the equivalent Nb content. However, the observed dependence of hydrostatic with crystallite orientation can be either associated to changes in Nb composition or to the presence of hydrostatic intergranular stresses. Without a complementary analysis, it is not possible to univocally identify its origin. For the extruded sample, the homogeneity of hydrostatic strain observed for all orientations within the main texture components suggest a compositional origin. On the other hand, for the cold rolled sample the large strain gradient observed within the main texture components suggests an additional contribution from intergranular stresses.

The magnitude of the intergranular stresses in the βZr phase was estimated by evaluating the SODF from the deviatoric strain tensor presented in Figures A3.1 (applying Hooke's law to the individual texture component) using the stiffness of Table 4. Figure 12 presents the resultant stresses for the cold rolled sample. As expected, the stresses for the extruded sample were below 100MPa for all the tensor components, and are not shown here. For the cold rolled sample, the deviatoric intergranular stresses vary in the range from (-600 to 400) MPa These values are higher than those obtained for the αZr phase, which range in the order of -350 to 200 MPa, as shown in Figure 8. It is important to mention that when fitting the model for αZr, it was imposed that the macro-stress must be zero.

The deviatoric strain and stress tensors of βZr grains for the different grain orientations are much more complex than those observed for αZr. In particular, the shear components are of similar magnitude than the diagonal terms, indicating that the principal axis differ from the principal direction of the tube (AD, HD and RD).

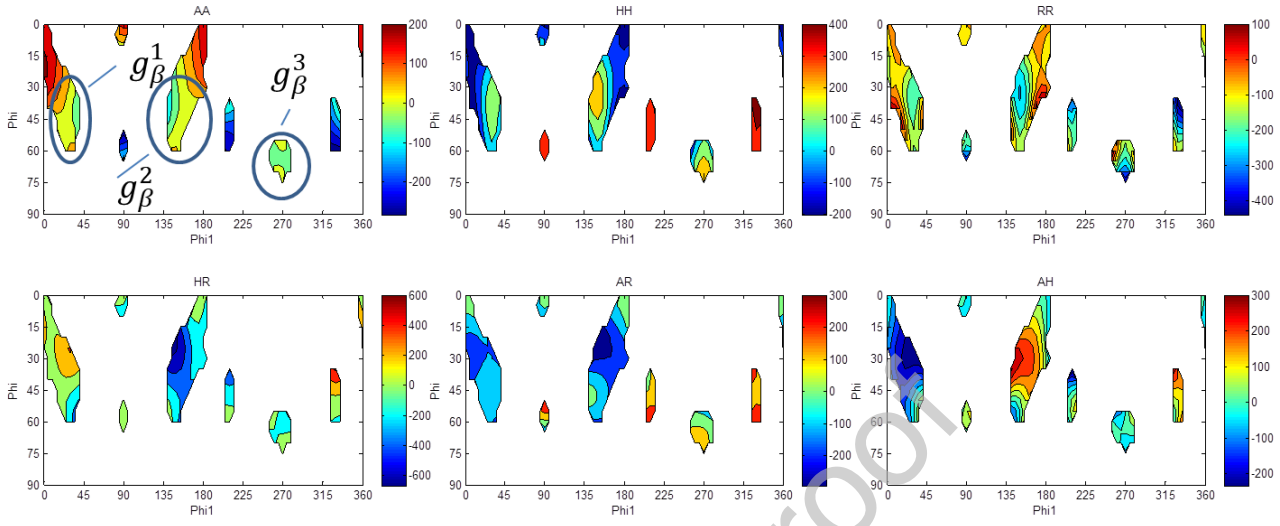

Figure 12: Deviatoric stress tensor for the cold rolled sample evaluated from the 6 component of the recalculated SODF of βZr for the cut Phi2=45°. The scales are in MPa.

Regarding the sample after autoclaving, the right column of Figure 7 presents the results of fitting the experimental SPF for ωZr, which shows only an acceptable agreement with the experimental data. However, since the orientation distribution function (ODF) of this phase is dominated by a single texture component, we have evaluated the stress state only for this specific orientation using the stiffness constant listed in Table 4. The resulting stress tensor is:

$$\sigma_{\omega Zr} = \begin{pmatrix} 57 & 29 & 32 \\ 29 & -163 & 26 \\ 32 & 26 & 6 \end{pmatrix} \pm 15MPa$$

All of the components, except for σ_{HH}, exhibit low values. Interestingly, σ_{HH} demonstrates a compressive character, which is compatible with the observed negative strain of the (0002) strain pole figure along the hoop direction.

5 Discussion

5.1 Evolution of texture during the process

One of the main results of this work is the determination of the evolution of the crystallographic texture of the minority phases at the different stages of the manufacturing process. However, it is worth mentioning the results obtained for the texture of the major αZr phase agrees completely with the literature [19,44, 45, 37]: the αZr is mainly determined during extrusion, and remains relatively stable through the remaining process, with only a small intensification of the m_{Hoop} orientation is observed due to the cold rolling process, as observed in Figure 2

For the minority βZr phase, it was observed that the texture is dominated by three main texture components: g_{β}^{1}, g_{β}^{2}, and g_{β}^{3}. The βZr texture does not show significant changes due to the cold rolling process and maintains a precise orientation relationship (Burger's orientation relationship) with the αZr texture. Similar to αZr, the texture of βZr is generated during the extrusion process and undergoes minor changes during cold rolling. An asymmetry between the upper and lower sections of the pole figures was observed, likely due to the shear forces exerted during the extrusion process by the surrounding αZr grains.

After the autoclaving process, βZr grains undergo decomposition into ωZr and an enriched β_{enr} phase, as evidenced by a decrease and a shift of all βZr peaks, and the emergence of several ωZr peaks. This prevents the definition of the ODF for the βZr phase in the material after autoclaving. However, the analysis of the evolution of the experimental pole figure of the only remaining βZr peak, (200), presented in Figure 4, indicates that decomposition of βZr grains depend on orientation, and occurs first in grains with the most prominent texture components, g_{β}^{1}, g_{β}^{2}, and g_{β}^{3}, suggesting an oriented selective process.

For the first time, the crystallographic texture of ωZr formed during heat treatment was determined, as shown in Figure 5. This texture is characterized by a single texture component, with an orientation that is consistent with ωZr grains coming from the decomposition of the main βZr texture components (g_{β}^{1}, g_{β}^{2}, and g_{β}^{3}). This result reinforces the notion that decomposition occurs first on β grains with the most frequent orientation, indicating that the kinetics of decomposition is orientation-dependent.

5.2 Implication of the presence of intergranular stresses

Hydrostatic stress is a crucial factor that affects the distribution of hydrogen (H) in solid solution, which in turn affects the formation of hydrides in the material during service. It is well-known that the presence of H causes elastic expansion of the crystal structure, making it less likely to find H in solid solution in grains under hydrostatic compression, and more likely to find higher concentrations in grains with tensile hydrostatic stress. At the service temperature of ~320ºC, where H uptake occurs, the stress field is expected to remain stable with respect to those presented in Figure 9. Therefore it is expected that in the cold rolled and autoclaving conditions H would tend to concentrate in grains with orientations close to g_{Radial}, where positive hydrostatic stresses occur, while avoiding orientations such as g_{Hoop}, where compressive-like hydrostatic stresses are present, This may affect the probability of hydride precipitation in grains with these orientations, favoring their formation in grains with g_{Radial} orientation and hindering their formation in those with g_{Hoop} orientation. This effect is expected to be reflected in the final texture of the hydride phase. The study by Vicente Alvarez et al. [37] presented the hydride texture of a heat-treated Zr2.5Nb pressure tube, and one of the key findings was that the probability of hydride precipitation increases as the c-axis of the grains rotates from the hoop to the radial direction, i.e., as the grain orientation changes from g_{Hoop} to g_{Radial}. This result is consistent with the conclusions drawn in the present work.

In reference to βZr, the experimental *d*-spacing of various diffraction peaks differs significantly from those of pure βZr. From the analysis of the strain pole figures, LSDF were obtained for this

phase for the extruded and cold rolled samples. The results for the different grain orientations were presented separated as hydrostatic contribution and deviatoric tensor contribution.

The hydrostatic strain present values of the order of ~10^4. As mentioned before, it is not possible without additional information to separate the effect of Nb content to that of hydrostatic intergranular stresses. Under the assumption that hydrostatic strains are predominantly induced by Nb content, Figure 11 illustrates that for both extruded and cold-rolled samples, the Nb content varies across grain orientations. Notably, the principal texture components exhibit the highest Nb content, approximately 2% more than the overall average. It is noteworthy that grains with the highest Nb content in solid solution are the ones undergoing the initial decomposition into ωZr during annealing (refer to Section 5.1). Clearly, a discernible correlation exists between these two observations. The kinetics of βZr decomposition during autoclaving is typically depicted using Time-Temperature-Transformation (TTT) diagrams. The presence of a higher Nb content in the grains may induce a shift in these lines towards shorter times, resulting in an earlier onset of decomposition.

In the extruded sample, the deviatoric stress tensor present values below 100MPa for all tensor components. After cold rolling, βZr grains experience a marked increase of the magnitude of intergranular stresses, much more than that observed for the major phase αZr. Depending on grain orientation a tensor component, stresses in the -600MPa to 400MPa range are estimated (see Figure 12). On the contrary, for αZr in the cold rolled condition intergranular stresses are lay within the -350MPa to +200MPa range (see Figure 8). This observation suggests that βZr grains experience higher plastic deformation and act as stress concentrators. This result is consistent with the findings of Ref[16] in which the authors investigated the evolution of the average strain in both αZr and βZr using neutron diffraction during tensile and compression tests.

The ωZr phase appear only after autoclaving, and the strain pole figures for this phase show values of magnitude below 1000 με, which are similar to those observed for αZr in the same processing condition. The texture of this phase is dominated by a single pole. After applying Hooke's law, the stress tensor for this main orientation could be estimated. The values obtained are low for all tensor components except for the HH component which ends with a slight compression of -160MPa. The origin of this stress is not clear, since is the result of the activation of several mechanisms including stress relaxation of parent βZr and transformation strains during ωZr formation.

Another significant implication arising from the existence of intergranular stresses is closely tied to the determination of crystal defects (such as dislocations, twins, and grain size) within the grain through analysis of diffraction line shapes. It is widely recognized that the physical broadening of diffraction peaks is influenced by the presence of defects. Various methods, including the Convolutional Multiple Whole Profile (CMWP), Warren Averbach, and Williamson-Hall techniques, are employed to estimate dislocation densities. As pointed out by Griffiths et al [57], this fact has prevented the determination of dislocation densities in cold worked pressure tubes because part of the line broadening is attributed to the interganular stresses. This phenomenon arises because the observed diffraction peak ultimately emerges as the composite outcome of diffraction peaks originating from individual grains oriented

differently (each with its respective *(hkl)* plane normal aligned parallel to the scattering vector). Within the context of intergranular stresses, these individual peaks might experience shifts, causing the collective average of these peaks to manifest as a broader, singular peak. Knowing the orientation distribution function of intergranular stress allows for a proper estimation of their impact on line broadening, yielding to a more accurate estimation of crystal defects.

5.3 Origin of Intergranular stresses

The section 4 presents results that reveal the presence of intergranular stresses in the polycrystal. However, interpreting the mechanisms that generate these stresses is not a straightforward task, as they arise from the complex interaction among the grains composing the material and are self-compensating to some extent. This difficulty increases when multiple phases are involved, as stresses can distribute differently not only along grains with different orientations but also across grains of different phases. Additionally, the shape of the grains (lamellae in this work, see Figure 1(e)) may also influence the stress distribution.

This work investigates intergranular stresses in three samples, each associated with distinct mechanisms. In the extruded sample, the material was deformed at high temperature (~800°C) and subsequently cooled down to room temperature. As a result, intergranular stresses at high temperature were negligible, and those observed at room temperature can be attributed to differences in thermal contraction between grains with different orientations (thermal stresses) [58]. In contrast, the cold-rolled sample exhibits intergranular stresses induced by the mechanically imposed deformation, which results in different responses from grains with various orientations and corresponding to different phases (deformation stresses). In the heat treated sample, the observed intergranular stresses arise from the relaxation of the deformation-induced stresses that developed during cold rolling. Overall, the three samples provide valuable insights into the various mechanisms that can give rise to intergranular stresses in polycrystalline materials, highlighting the importance of understanding the underlying processes to design and engineer materials with desired properties.

Prediction of the observed intergranular stresses needs micromechanical modeling of the polycrystalline ensemble. An example of this type of model is the elasto-vicsoplastic model developed by Turner and Tome [54]. In this model, the grains are modeled as an inclusion in a medium, whose response is self-consistently evaluated. The texture of the material is incorporated through the medium, while the elasto-plasctic response of the inclusion depends on the activation of the different slip and twinning modes. While the solution of this problem is not straightforward, it is possible to obtain it using specialized programs that are outside the scope of this work. Nevertheless, the results presented in this study provide valuable insights for calibrating and validating micromechanical models of this type.

6 Conclusions

Crystallographic texture and intergranular stresses are crucial factors in determining the properties and performance of polycrystalline materials. In Zr alloys, the coexistence of hydrogen and stresses can trigger a degradation mechanism, known as delayed hydride cracking, leading to catastrophic failure. While the crystallographic texture of the majority αZr phase is

well documented, this study presents, for the first time, the evolution of the crystallographic texture of the minority βZr and ωZr phases in a Zr2.5Nb pressure tube under three different processing conditions: extruded, cold rolled, and after autoclaving. It is also presented for the first time the map of the intergranular stresses of αZr, βZr and ωZr as a function of grain orientation and how they are affected during the fabrication process. The dependence of these stresses with grain orientation were determined by analyzing the lattice strain pole figures, which were obtained through high-energy synchrotron X-ray diffraction experiments conducted at the Advanced Photon Source using transmission geometry.

It was found that the texture of the βZr phase changes only slightly after cold rolling, and the Burgers orientation relationship between the αZr and βZr phases remains intact. After autoclaving, certain βZr grains decompose first, and grains corresponding to the ωZr phase are formed. The texture of the ωZr precipitates is dominated by a single component that follows the β(111)//ω(0001) and β<-110)>//ω<11-20> orientation relationship with the first βZr grains to decompose. The Nb concentration in solid solution was found to increase from 20 at% to 50 at% after heat treatment.

The methods to obtain the intergranular stresses from the SPF are based in the Fourier expansion of the strain tensor coefficients. In this work, an optimized methodology is proposed to obtain orientation distribution of intergranular stresses from the strain pole figures, which is done by expanding the distributions into symmetrized Fourier functions of the Euler space and fitting the Fourier coefficients of the expansion using a least squares method.

The intergranular stresses in αZr grains after extrusion were found to be low, below 60 MPa. However, the rolling process leads to a significant increase in intergranular stresses, with maximum values reaching 200 MPa to -350MPa, and a strong dependence on grain orientation. The post-autoclaving treatment effectively produces stress relaxation, but the dependence of these stresses on grain orientation persists. For the cold-rolled and post-annealed samples, the hydrostatic stress is tensile for grain orientations with their c-axis along the radial direction and compressive for those grains oriented with their c-axis along the hoop direction. The abnormal dependence of precipitation probability of hydrides with grain orientation observed in this material can be explained by a reduction of H in content in solid solution due to the presence of tensile type hydrostatic stresses.

The βZr phase grains exhibit significant intergranular strains in both the extruded and cold-rolled conditions. The hydrostatic part of this strain was associated with a variation in the content of Nb in solid solution. It was observed that those βZr grains with the most frequent orientations present higher hydrostatic strain, that was associated to higher amount of Nb in solid solution. At the same time, these grains decompose first into ωZr during annealing, suggesting that there is a relation between the kinetic of βZr decomposition and the content of Nb in solid solution. On the other hand, deviatoric strains were associated with intergranular stresses. For the extruded sample, these stresses are below 80 MPa, while for the cold-rolled condition, they increase to values of -600 to 400 MPa, much higher than those observed for αZr. This is attributed to a higher degree of deformation of this phase and its role as a stress concentrator. Overall, this

study provides valuable insights into the crystallographic texture and intergranular stresses of Zr alloys and their effects on the material's properties and performance.

APPENDIX I : LSDF and SODF Inversion method

In this appendix a description of the main steps to obtain the expressions of the strain pole figures as a function of the Fourier parameters of the strain tensor components is presented. In this work, the Fourier expansion of the ODF and the strain tensor components is done on a symmetrized basis that fulfills with the crystal symmetry and the strain field symmetry. This new methodology permits reduce considerably the number of parameters during the fitting of the strain pole figures. Also, with this basis the representation of the LSDF and the SODF end defined in the fundamental region of the Euler space.

Fourier expansion was used by different authors ([23-27,29,30, 32-33]) using non-symmetrized Jacobi augmented functions Z_{lmn} to perform analytical integration of Eq.(1). Only Behnken utilized symmetrized generalized spherical harmonics [28] as defined in the book by Bunge for the expansion [40], however in his work integration over $g_{\perp}$ was carried out numerically. Popa and Balzar [31] took a different approach by defining the weighted strain ODF as the product of $\varepsilon_g{}' = \varepsilon_g(\rho,\phi)f(g)$ and transformed Eq.(1) to a problem similar to that of quantitative texture analysis (QTA) by multiplying $\varepsilon_{hkl}(\rho,\phi)$ by the denominator $(\int_{g_{\perp}} f(g).dg)$. The resulting quantities were expanded in generalized spherical harmonics, and a similar linear system was obtained that links the SPF and the Fourier coefficients of $\varepsilon_g{}'$.

In this study, the approach introduced by Wang et al.in Ref[23] was adopted but employ the symmetrized generalized spherical harmonics described in Bunges's book [40] as expansion functions. Unlike the method proposed by Behnken, the integration in Eq.(1) was performed analytically. A detailed derivation of the SPF expression in terms of these functions is provided here for clarity.

Following Bunge [40], $f(g)$ can be expanded in a series of symmetrized generalized spherical harmonics $T_{l\mu\nu}^{CS,SS}$:

$$f(g) = \sum_{l=0} \sum_{\mu=1}^{M(l)} \sum_{\nu}^{N(l)} C_{l\mu\nu} T_{l\mu\nu}^{CS,SS}(g) \quad \text{(A1)}$$

where *CS* and *SS* refer to crystal and sample symmetry, respectively, $C_{l\mu\nu}$ are the Fourier coefficients and summations run from *1* to $M(l)$ and $N(l)$. Functions $T_{l\mu\nu}^{CS,SS}$ are evaluated as a linear combination of the non-symmetrized generalized spherical harmonics T_{lmn} as:

$$T_{l\mu\nu}^{CS,SS}(g) = \sum_{m=-l}^{l} \sum_{n=-l}^{l} A_{l,m\mu}^{CS} A_{l,n\nu}^{SS} T_{lmn}(g) \quad \text{(A2)}$$

Functions T_{lmn} are a generalization of the associated Legendre functions and are defined in Chapter 14 of Ref [40] . Coefficients $A_{l,m\mu}^{CS}$ and $A_{l,n\nu}^{SS}$ depend on the crystal and sample symmetry, respectively. Using symmetrized functions provides two advantages: 1) it allows for

the reduction of the Euler space to the fundament region, and 2) there is a significant decrease in the total number of functions $T_{l\mu\nu}^{CS,SS}$ required to expand the ODF when compared to the non-symmetrized case, where this number increases as $(2l+1)^2$ for each *l*. The definition of coefficients $A_{l,m\mu}^{CS}$ for hexagonal, orthorhombic, tetragonal, and cylindrical symmetry can be found in Table 14.4 of Ref[40], while the coefficients for cubic symmetry are listed in Table 15.2.2 of Ref[40] and also in Refs[41, 42].

In a similar way, strain tensor components can be expanded in these functions:

$$\varepsilon_{ij}^{g}(g) = \sum_{l=0} \sum_{\mu=1}^{M(l)} \sum_{\nu}^{N(l)} E_{l\mu\nu}^{ij} T_{l\mu\nu}^{CS,SS}(g) \quad \text{(A3)}$$

In this expression $E_{l\mu\nu}^{ij}$ are the Fourier coefficients l μ ν of the *ij* component of the strain tensor. It is important to note that the sample symmetry *SS* does not correspond to the texture of the material but rather represents the lower symmetry that is shared by both the texture and the strain field.

By substituting Eq.(A2) and (A3) into Eq.(1), the integral can be analytically evaluated, leading to the following expression for the SPF:

$$\varepsilon_{hkl}(\rho,\phi) = \sum_{ij} \propto_i \propto_j \sum_{\substack{l\mu\nu \\ l_\varepsilon\mu_\varepsilon\nu_\varepsilon}} \mathrm{C}_{l\mu\nu} E_{l_\varepsilon\mu_\varepsilon\nu_\varepsilon}^{ij} \sum_{l_1=|l_\varepsilon-l|}^{|l_\varepsilon+l|} \sum_{\mu_\varepsilon\nu_\varepsilon} \{ll_\varepsilon\mu\mu_\varepsilon|l_1\mu_1\}^{CS} \{ll_\varepsilon\nu\nu_\varepsilon|l_1\nu_1\}^{SS} \frac{8\pi^2}{(2l_1+1)} k_{l_1\mu_1}^{CS}(\hat{h})^* k_{l_1\nu_1}^{SS}(\hat{\tau}) \Big/ \left(\sum_{l\mu\nu} \mathrm{C}_{l\mu\nu} \frac{8\pi^2}{(2l_1+1)} k_{l\mu}^{CS}(\hat{h})^* k_{l\nu}^{SS}(\hat{\tau}) \right) \quad \text{(A4)}$$

where $\{ll_\varepsilon\mu\mu_\varepsilon|l_1\mu_1\}^{CS}$ are the symmetrized version of the Clebsch-Gordon coefficients and $k_{l\mu}^{CS}(\hat{x})$ are the symmetrized surface spherical harmonics. In this equation $\hat{h}$ represents the direction of the (*hkl)* plane normal in the crystal reference system, while $\hat{\tau}$ is the direction of the scattering vector in the sample reference system (corresponding to angles *(ρ, ϕ)* of the pole figures). By utilizing Eq.(A4), the Fourier coefficients of the strain tensor $E_{l_\varepsilon\mu_\varepsilon\nu_\varepsilon}^{ij}$ can be obtained from the experimental SPF through linear inversion.

The stress tensor components can also be expanded using the functions $T_{l\mu\nu}^{CS,SS}$ with coefficients $\Gamma_{l\mu\nu}^{ij}$, similar to the expansion of the strain tensor. Furthermore, the stiffness tensor components can be expressed as a linear combination of generalized spherical harmonics of order up to *l=4*, as demonstrated in Refs [40]. As both strain and stress exhibit sample symmetry, the stiffness tensor in Eq.(3) must also satisfy sample symmetry for Hooke's relation to be valid. Consequently, the stiffness tensor can be expanded in terms of symmetrized generalized spherical harmonics of the type $T_{l\mu\nu}^{CS,SS}$, with coefficients $Q_{l_s\mu_s\nu_s}^{ijkl}$. Therefore, Eq.(3) can be transformed into a relation between the Fourier coefficients of the stress and strain tensor components:

$$\Gamma^{ij}_{l\mu\nu} = \sum_{kq} \sum_{\substack{l_s\mu_s\nu_s \\ l_\varepsilon\mu_\varepsilon\nu_\varepsilon}} Q^{ijkq}_{l_s\mu_s\nu_s} E^{kl}_{l_\varepsilon\mu_\varepsilon\nu_\varepsilon} \{l_s l_\varepsilon \mu_s \mu_\varepsilon | l\mu\}^{CS} \{l_s l_\varepsilon \nu_s \nu_\varepsilon | l\nu\}^{SS} \quad \text{(A5)}$$

Eq.(A5) provides a direct method for computing the Fourier coefficients of the stress tensor, given that those of the strain tensor have been determined.

Several authors have pointed out that in order to obtain reliable results from the least square minimization of Eq.(A4) to the experimental SPF, certain extra conditions on the strain/stress fields should be assumed, taking into account the errors of the experimental data, the number of SPF used and their coverage. Wang et al. proposed a misfit function that quantifies the deviation of the estimated states of stress and strain from the self-consistent solution of grains embedded in a homogeneous medium [23]. Behnken introduced several additional conditions, such as the minimization of stress, strain, and energy variances as a function of grain orientation, and some other physical considerations [28]. Bernier and Miller suggested the minimization of the integrated value of the gradient of the strain field and the trace of the strain field over the whole fundamental region of the Euler space [29]. All of these conditions make the minimization of Eq.(A4) a non-linear problem.

This model was implemented in MATLAB, utilizing various functions from the MTEX library [43]. In order to program the symmetrized generalized spherical harmonics, we followed the convention described in Bunge's book [40]. Rather than coding the T_{lmn} functions using their expression in terms of the three Euler angles (ϕ_1, Φ, ϕ_2), we utilized the Wigner functions that were already defined in the MTEX toolbox, taking advantage of MTEX's capabilities to facilitate fast Fourier coefficient evaluation. Similarly, we defined the symmetrized surface spherical harmonic functions $k^{CS}_{l\mu}$. The symmetrized Fourier coefficients $C_{l\mu\nu}$ of functions $T^{CS,SS}_{l\mu\nu}$ were also defined in this way. Additionally the symmetrized version of the Clebsch-Gordon coefficients were programmed, which were evaluated using the non-symmetrized version included in MTEX. The LSQNLIN subroutine of MATLAB was used for minimization purposes.

APPENDIX II: SODF of α-Zr

In this appendix, the results obtained for the SODF of the αZr phase are presented. The cut with Phi1=0 is shown since there appear the main texture components of this phase. Each panel contains 6 Figures corresponding to the 6 stress tensor components in the sample reference system (AD, HD and RD).

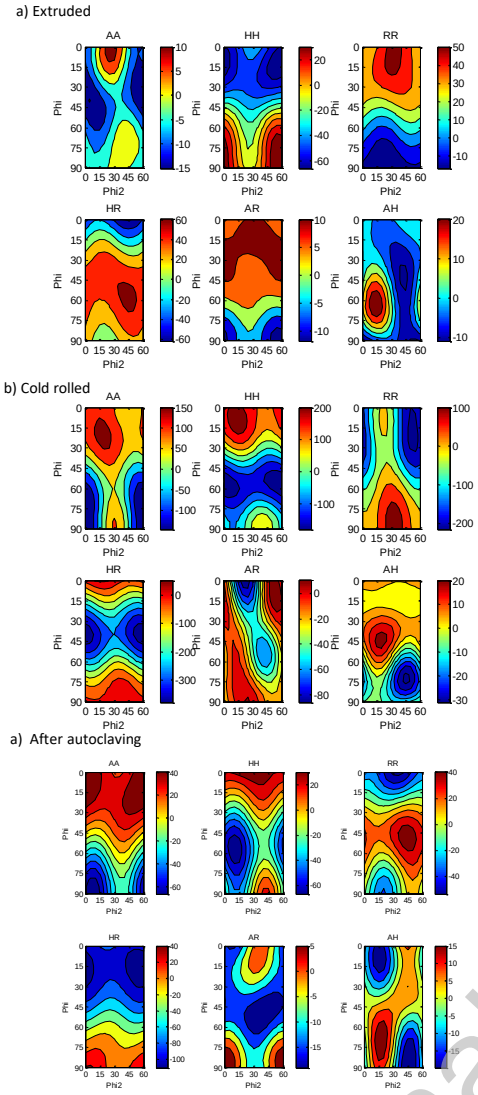

Figure A2.1: Phi1=0 section of the SODF of αZr for the 6 tensor components for (a) Extruded sample (b) cold rolled sample (c) Autoclaved sample. The colour scales give stress values in MPa.

APPENDIX III: LSDF of β-Zr

In this appendix, the results obtained for the deviatoric part of the LSDF of the βZr phase are shown for the extruded and cold rolled samples. Only, the cut with Phi1=45^{o} is presented, where the three main texture components can be clearly identified. For visualization purposes only those orientations with intensity in MRD higher than 20% of the maximum value of the ODF are shown, while the results for other orientations appear as white regions.. The volume fraction of all these orientations represents 40% of the total material Each panel contains 6 Figures corresponding to the 6 stress tensor components in the sample reference system (AD, HD and RD).

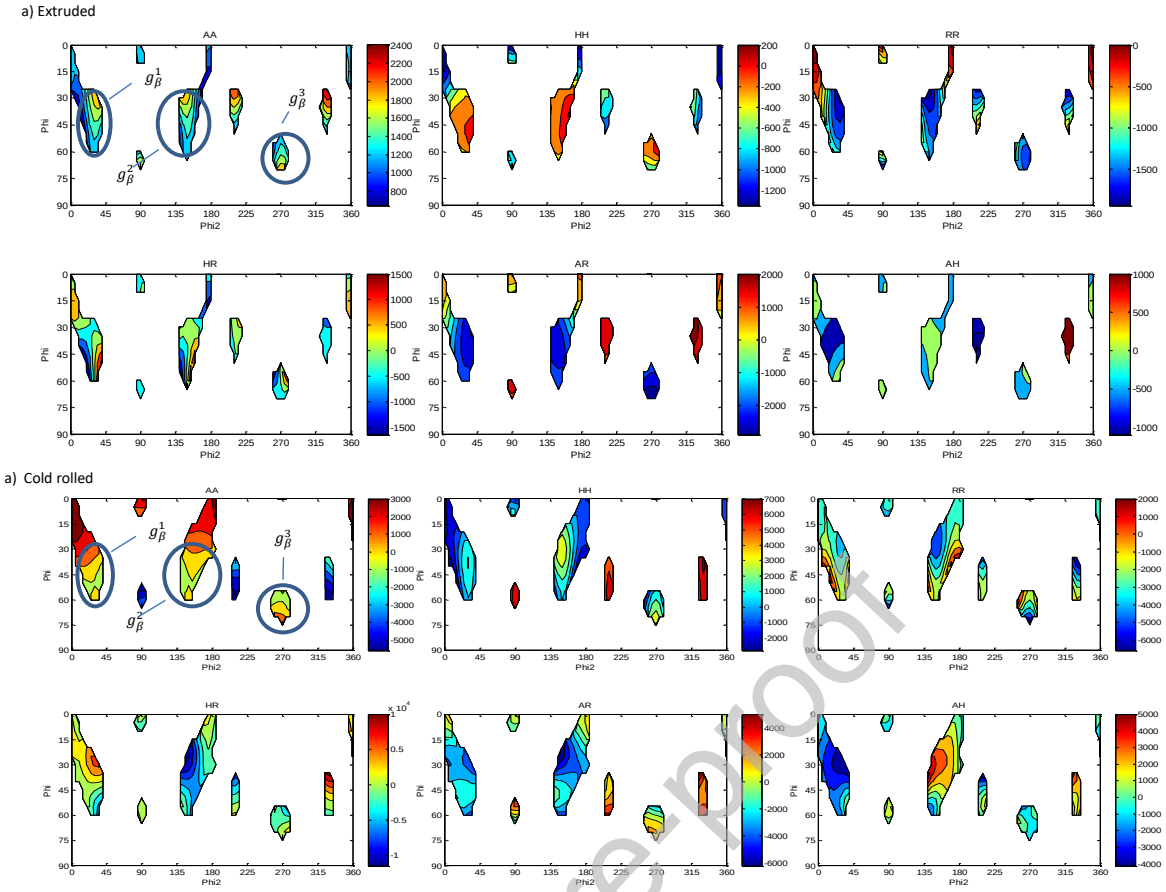

Figure A3.1: Phi2=45° section of the LSDF of βZr for the 6 components of the deviatoric part of the strain tensor for the (a) extruded and (b) cold rolled samples. Only the results for the most representative texture components are depicted. The colour scale gives strain in με.

References

[1] R. B. Adamson, C.E. Coleman, M. Griffiths, Irradiation creep and growth of zirconium alloys: A critical review, Journal of Nuclear Materials, Volume 521, 1 August 2019, Pages 167-244

[2] R.N. Singh , Niraj Kumar, R. Kishore, S. Roychaudhury, T.K. Sinha, B.P. Kashyap, Delayed hydride cracking in Zr–2.5Nb pressure tube material, Journal of Nuclear Materials, Volume 304, Issues 2–3, August 2002, Pages 189-203.

[3] D.O. Northwood, U. Kosasih, Hydrides and delayed hydrogen cracking in zirconium and its alloys, Int. Met. Rev., 28 (2) (1983), p. 92

[4] J.R. Theaker, R. Choubey, G.D. Maon, S.A. Aldridge, L. Davis, R.A. Graham, C.E. Coleman, Fabrication of Zr-2.5Nb Pressure Tubes to Minimize the Harmful Effects of Trace Elements, Zirconium in Nuclear Industry: 10th International Symposium, ASTM-STP-1245 (1994) 221

[5] R.N. Singh, R. Kishore, T.K. Sinha, B.P. Kashyap, Hydride blister formation in Zr–2.5 wt% Nb pressure tube alloy,J. Nucl. Mater., 301 (2002), p. 153

[6] C.E. Coleman, Susceptibility of cold-worked zirconium-2.5 wt% niobium alloy to delayed hydrogen cracking, AECL-5260 (1976) 1

[7] B. Cox, Environmentally-induced cracking of zirconium alloys—A review, J. Nucl. Mater., 170 (1990), p. 1

[8] S.S. Kim, S.C. Kwon, Y.S. Kim, The effect of texture variation on delayed hydride cracking behavior of Zr–2.5% Nb plate,J. Nucl. Mater., 273 (1999), p. 52

[9] S. Sagat, C.K. Chow, M.P. Puls, C.E. Coleman, Delayed hydride cracking in zirconium alloys in a temperature gradient ,J. Nucl. Mater., 279 (2000), p. 107

[10] C.E. Coleman, B.A. Cheadle, J.F.R. Ambler, P.C. Lichtenberger, R.L. Eadie, Minimizing hydride cracking in zirconium alloys, Can. Metall. Q, 24 (3) (1985), p. 245

[11] V. Perovic, G.C. Weatherly, R.G. Fleck, Characterization of dislocation substructures in Zr-2.5 Nb pressure tube alloys, Can. Metall. Q, 24 (3) (1985), p. 253

[12] Assessment and Management of Ageing of Major Nuclear Power Plant Components Important to Safety: CANDU Pressure Tubes, IAEA 1998 TECDOC-1037 (Austria: INIS Clearinghouse)

[13] E. Tenckhoff in Deformation mechanism, texture, and anisotropy in zirconium and zircaloy STP 966, American Society for Testing and Materials, (1988)

[14] B.A. Cheadle, C.E. Ells, W. Evans, The development of texture in zirconium alloy tubes, Journal of Nuclear Materials Vol 23 Issue 2 (1967) 199-208

[15] C. Daniel, P. Honniball,, L. Bradley, M. Preuss, Texture Development during Rolling of $\alpha + \beta$ Dual-Phase ZrNb Alloys,in Zirconium in the Nuclear Industry: 18th International Symposium 151-179.

[16] S. Cai , M. Daymond, R.A. Holt , M.A. Gharghouri , E.C. Oliver, Evolution of interphase and intergranular stresses in Zr–2.5Nb during room temperature deformation, Materials Science and Engineering A 501 (2009) 166–181

[17] R.W.L. Fong, R. Miller, H.J. Saari, S.C. Vogel Crystallographic Texture and Volume Fraction of α and β Phases in Zr-2.5Nb Pressure Tube Material During Heating and Cooling, Metallurgical and Materials Transactions A, 43A (2012) 806-821.

[18] M. Griffiths , J.E. Winegar, A. Buyers, The transformation behaviour of the β-phase in Zr–2.5Nb pressure tubes, Journal of Nuclear Materials 383 (2008) pp. 28–33

[19] R.A. Holt, In-reactor deformation of cold-worked Zr–2.5Nb pressure tubes, J. Nucl. Mater., 372 (2008), 182-214

[20] G. Juarez, C. P. Buioli, A.V. Flores, M. Dellagnolo; J.R. Santisteban, M. A. Vicente Alvarez, D. Azzinar, D. Bianchi, A. Revesz, M. Hoffman, T. Ungar, P. Vizcaino. Evolución de la textura cristalina en los procesos de fabricación de combustibles y componentes internos de reactores nucleares de potencia, Ciencia e Investigación; Lugar: Buenos Aires, Vol 1 (2019) 5 – 32.

[21] M. A. Meyers, K. Kumar Chawla in Mechanical Metallurgy: Principles and Application , Prentice-Hall, Inc.; First Edition (January 1, 1983).

[22] E. Kula, V.. Weiss, Residual Stress and Stress Relaxation, Sagamore Army Materials Research Conference Proceedings, Springer 1982

[23] Y. D. Wang, R. Lin Peng, R.L. McGreevy, A novel method for constructing the mean field of grain-orientation-dependent residual stress, Philosophical Magazine Letters, Vol. 81 N°3 (2001) 153-163.

[24] Y. D. Wang, X.L. Wang, A. D. Stoica, J. W. Richardson, R. Lin Peng, Determination of the stress orientation distribution function using pulsed neutron sources, Journal of Applied Crystallography, 2002.

[25] Y. D. Wang, R Lin Peng, X. -L.Wang, R.L. McGreevy, Grain-orientation-dependent residual stress and the effect of annealing in cold-rolled stainless Steel, Acta Materialia 50 (2002), 1717-1734.

[26] E. Demir, J.-S. Park, M.P. Miller, P.R. Dawson, A computational framework for evaluating residual stress distributions from diffraction-based lattice strain data, Comput. Methods Appl. Mech. Engrg. 265 (2013) 120–135.

[27] K. P. McNelis, P. R. Dawson, M. P. Miller, A two-scale methodology for determining the residual stresses in polycrystalline solids using high energy X-ray diffraction data, Journal of the Mechanics and Physics of Solids 61 (2013) 428–449

[28] H. Behnken, Strain-Function Method for the Direct Evaluation of Intergranular Strains and Stresses, Pphys. Stat. Sol. (a) Vol 177, (2000), 401-418

[29] J. V. Bernier, M. P. Miller, A direct method for the determination of the mean orientation-dependent elastic strains and stresses in polycrystalline materials from strain pole figures, J. Appl. Cryst. Vol 39 (2006), 358–368.

[30] M. P. Miller, J. V. Bernier, J.-S. Park, and A. Kazimirov, Experimental measurement of lattice strain pole figures using synchrotron x rays, Review of Scientific Instruments 76, (2005), 113903.

[31] N. C. Popa and D. Balzar, Elastic strain and stress determination by Rietveld refinement: generalized treatment for textured polycrystals for all Laue clases, J. Appl. Cryst.. 34, (2001) 187-195.

[32] C. Larsson ,B. Clausen, T.M. Holden, M.A.M. Bourke, Measurements and predictions of strain pole figures for uniaxially compressed stainless Steel, Scripta Materialia 51 (2004) 571–575.

[33] M.P. Miller, J.-S. Park, P.R. Dawson, T.-S. Han, Measuring and modeling distributions of stress state in deforming Polycrystals, Acta Materialia 56 (2008) 3927–3939.

[34] D. Juul Jensen, H.F. Poulsen. The three dimensional X-ray diffraction technique, Materials Characterization 72 (2012) 1–7.

[35] K. Kapoor, D. Lahiri, C. Padmaprabu, T. Sanyal, X-ray measurement of near surface residual stress in textured cold-worked stress-relieved Zr–2.5%Nb pressure tube material, Journal of Nuclear Materials 303 (2002) 147–155.

[36] 1-ID Home Page | Advanced Photon Source (anl.gov)

[37] M.A. Vicente Alvarez , J.R. Santisteban , G. Domizzi , J. Almer , Phase and texture analysis of a hydride blister in a Zr–2.5%Nb tube by synchrotron X-ray diffraction, Acta Materialia 59 (2011) 2210–2220

[38] M.A. Vicente Alvarez, J.R. Santisteban, P. Vizcaino, A.V. Flores, A.D. Banchik, J. Almer, Hydride reorientation in Zr2.5Nb studied by synchrotron X-ray diffraction, Acta Materialia 60 (2012) 6892–6906.

[39] P. Vizcaíno, J.R. Santisteban, M.A. Vicente Alvarez, A.D. Banchik, J. Almer, Effect of crystallite orientation and external stress on hydride precipitation and dissolution in Zr2.5%Nb, Journal of Nuclear Materials 447 (2014) 82–93,

[40] H. J. Bunge in Texture Analysis in Materials Science, 1993

[41] R.R. Morris, Generalized spherical harmonics for cubic-triclinic symmetry,Texture and Microstructures, Vol. 24, (1995) 221-224.

[42] J. Muggli, Cubic harmonics as linear combinations of spherical harmonics, Journal of Applied Mathematics and Physics (ZAM P), Vol 23, (1972) 311-317.

[43] R Hielscher , H. Schaeben, A novel pole figure inversion method: specification of the MTEX algorithm, Journal of Applied Crystallography vol 41 (2008) 1024-1037.

[44] R.A. Holt, S.A. Aldridge, Effect of extrusion variables on crystallographic texture of Zr-2.5 wt% Nb, J. Nucl. Mater. 135 (1985) 246-259.

[45] R.A. Holt, P. Zhao, Micro-texture of extruded Zr–2.5 Nb tubes, J. Nucl. Mater. 335 (2004) 520-528.

[46] G.K. Dey, S. Banerjee, Decomposition of the β-phase in Zr-20%Nb, Journal of Nuclear Materials 125 (1984) 219-227.

[47] H.-R. Wenk, P. Kaercher, W. Kanitpanyacharoen, E. Zepeda-Alarcon, Y. Wang, Orientation Relations During the α–ω Phase Transition of Zirconium: In Situ Texture Observations at High Pressure and Temperature, PRL 111, (2013) 195701-5.

[48] R. Tewari, D. Srivastava , G.K. Dey , J.K. Chakravarty , S. Banerjee , Microstructural evolution in zirconium based alloys, Journal of Nuclear Materials 383 (2008) 153–171.

[49] R. W. G Wyckoff, Second edition. Interscience Publishers, New York, New York Hexagonal closest packed, hcp, structure, Crystal Structures, Vol 1 (1963) 7-83.

[50] G.B. Grad, J.J. Pieres, A.F. Guillermet, G.J. Cuello, R.E. Mayer, J.R. Granada, Lattice parameter of the Zr-Nb bcc phase: neutron scattering study and assessment of experimental data Zeitschrift fuer Metallkunde vol. 86(6) (1995) 395-400,

[51] Y. S. Kim, S. S. Kim, Y. M. Cheong, K. S. Im, Determination of dislocation density and composition of β-Zr in Zr–2.5Nb pressure tubes using X-ray and TEM, Journal of Nuclear Materials 317 (2003) 117–129

[52] G.B. Grad, J.J. Pieres, A. Fernamdez Guillermet, G.J. Cuello, J.R. Granada, R.E. Mayer, Systematics of lattice parameters and bonding distances of the omega phase in Zr-Nb alloys, Physica B 213&214 (1995) 433-435

[53] S. Zhang , X. Zhang , Y. Zhu , S. Zhang , L. Qi , R. Liu, First-principles investigations on elastic and thermodynamic properties of zirconium under pressure, Computational Materials Science 61 (2012) 42-49

[54] P.A. Turner, C. N. Tome, A study of residual stresses in Zircaloy-2 with rod texture, Acta Metall, Mater. Vol. 42, No. 12, (1994)4143~1153,

[55] Causey, A.R. «Anisotropy of irradiation creep of Zr-2.5wt%Nb and Zircaloy-2 alloys». Journal of Nuclear Materials 98, n.º 3 (junio de 1981): 313-21. https://doi.org/10.1016/0022-3115(81)90157-4

[56] Kocks, Texture and anisotropy, Kocks, U. F. Texture and Anisotropy: Preferred Orientations in Polycrystals and Their Effect on Materials Properties. Cambridge University Press, 2000.

[57] Griffiths, M., D. Sage, R. A. Holt, and C. N. Tome. Determination of Dislocation Densities in HCP Metals from X-Ray Diffraction Line-Broadening Analysis. Metallurgical and Materials Transactions A33, (2002): 859-65.

[58] D. G. Carr, M. I. Ripley, D. W. Brown, S.C. Vogel, and T. M. Holden, Residual stress measurement on a stress relieved Zircaloy-4 weld by neutron diffraction, Journal of Nuclear materials 359, (2006) 202-207.

Acknowledgement

This work was partially supported by AGENCIA NACIONAL DE PROMOCIÓN DE LA INVESTIGACIÓN, EL DESARROLLO TECNOLÓGICO Y LA INNOVACIÓN through PICT-2021-I-A-00094. This research used resources of the Advanced Photon Source, a US Department of Energy (DOE) Office of Science User Facility operated for the DOE Office of Science by Argonne National Laboratory under contract No. DE-AC02-06CH11357. We want to thank J. Almer and J. Okasinski for assisting during the experiment at APS.

Graphical abstract

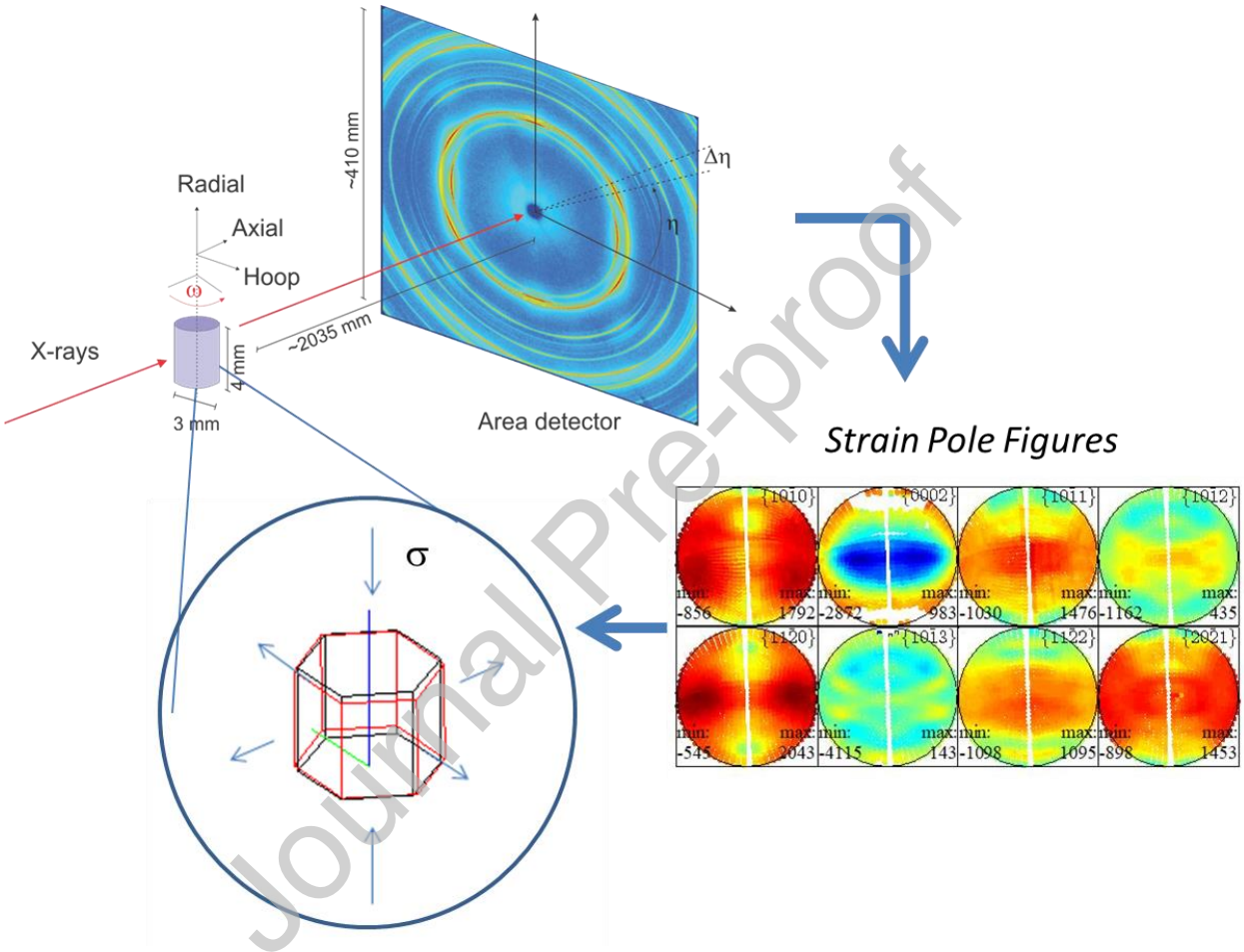

Declaration of interests

☒ The authors declare that they have no known competing financial interests or personal relationships that could have appeared to influence the work reported in this paper.

☐The authors declare the following financial interests/personal relationships which may be considered as potential competing interests: